From axion inflation to turbulence

Abstract.

Using 2+1 dimensional numerical simulations, we study the emergence of the radiation dominated era of the early universe when the inflaton decays into radiation and, at the same time, drives magnetic fields. This intricate process changes the way how the magnetic field decays during the radiation limited era. Bulk motions of the plasma play an important role in driving the inverse cascade of the magnetic field toward larger length scales. We show that a significant amount of kinetic energy can be driven during the decay of the inflaton field. This changes the magnetic decay from a magnetically to kinetically dominated one, which is no longer fully controlled by the approximate magnetic helicity conservation. During the reheating era, there is sustained driving of turbulent electromagnetic energy from the inflaton. This modifies the inverse cascade and suppresses the forward cascade. Once the inflaton has decayed, the electromagnetic energy can only decrease and the forward cascade is no longer suppressed. This leads to a distinct change in the inverse cascade between the reheating and subsequent radiation-dominated epochs.

(July 23, 2026)

Contents

1 Introduction

Axion inflation provides a possible means of amplifying magnetic fields from quantum fluctuations through the Chern-Simons coupling of a pseudoscalar axion-like field to gauge fields [1–5]. Toward the end of inflation, Schwinger pair production leads to an electrically conducting plasma [6–9]. Viscous and resistive heating processes provide an early source of radiative energy. During the reheating era, the decay of the inflaton contributes the main part of radiative heating until the inflaton has fully decayed. By that time, the system is fully described by the equations of magnetohydrodynamics (MHD), when the displacement current has become unimportant.

Schwinger pair production leads to electric currents and a nonvanishing Lorentz force that drives bulk motions in the plasma. Those motions are turbulent and affect the magnetic field evolution. They produce not only an accelerated decay of the magnetic field, but they can also transfer magnetic energy to progressively larger length scales [10]. This process of turbulent decay has previously been studied either in isolation without the underlying magnetogenesis that produces the magnetic field [11–14], or under rather simplifying assumptions about the emergence of a conducting plasma [15–18].

Here we study the MHD evolution of a radiation-dominated plasma in combination with the magnetogenesis process. We do this by extending recent lattice simulations of Schwinger currents in gauge-field preheating simulations [19]. In the present work, however, we include the evolutionary equations for the plasma bulk motions and its viscous and resistive heatings as well as the decay of the inflaton. To enable a broad exploration of relevant parameter regimes, we focus here on two-dimensional simulations.

Our paper is structured as follows. We motivate our model in detail in section 2. In particular, we discuss the flow of energies between the relevant energy reservoirs and state the governing equations. In section 3, we present our results both visually in real space and in terms of spectra, and compare models with different axion masses. We discuss the results in an evolutionary diagram of characteristic comoving magnetic field strengths versus comoving characteristic length scale. We conclude in section 5.

We use Planck units by setting $G = \hbar = c = k_{\rm B} = 1$. Electromagnetic quantities are expressed in Lorentz-Heaviside units. We use comoving quantities for most fields, except for the inflaton field. We denote all other physical fields with the superscript "ph".

2 The model

2.1 Basic equations

In this paper, we couple the equations of axion inflation with those of magnetohydrodynamics (MHD), which provides the relevant description of the plasma in the radiation dominated era. We employ the conformal time $\tau = \int \mathrm{d}t/a(t)$, where t is the cosmic time and $a(t)$ is the scale factor of the universe. It is convenient to work with comoving electric and magnetic fields, $\boldsymbol{E}$ and $\boldsymbol{B}$, respectively. They are related to the physical fields via $\boldsymbol{E} = a^2\boldsymbol{E}_{\rm ph}$ and $\boldsymbol{B} = a^2\boldsymbol{B}_{\rm ph}$. Likewise, the comoving radiation energy density, ρ, which includes the rest mass energy density, is related to the physical one via $\rho = a^4\rho_{\rm ph}$. The comoving and physical bulk velocities of the plasma are the same as the physical one and denoted by $\boldsymbol{u}$ $(= \boldsymbol{u}_{\rm ph})$. When using comoving variables and conformal time, the scale factor drops out of the MHD equations

[10]. For the axion field, ϕ, on the other hand, it is more convenient to work with the physical field. We therefore drop the subscript "ph" on ϕ. Thus, our full system of evolution equations for ϕ, $\boldsymbol{E}$, $\boldsymbol{B}$, $\boldsymbol{u}$, ρ, and a is

$$\frac{\partial^2\phi}{\partial\tau^2} + (2\mathcal{H} + a\Gamma_\phi)\frac{\partial\phi}{\partial\tau} - \boldsymbol{\nabla}^2\phi + a^2\frac{dV}{d\phi} = a^{-2}\frac{\alpha}{f}\boldsymbol{E}\cdot\boldsymbol{B}, \tag{2.1}$$

$$\frac{\partial\boldsymbol{E}}{\partial\tau} = \boldsymbol{\nabla}\times\boldsymbol{B} - \frac{\alpha}{f}\left(\frac{\partial\phi}{\partial\tau}\boldsymbol{B} + \boldsymbol{\nabla}\phi\times\boldsymbol{E}\right) - \boldsymbol{J}, \tag{2.2}$$

$$\frac{\partial\boldsymbol{B}}{\partial\tau} = -\boldsymbol{\nabla}\times\boldsymbol{E}, \tag{2.3}$$

$$\tfrac{4}{3}\rho\left(\frac{\partial\boldsymbol{u}}{\partial\tau} + \boldsymbol{u}\cdot\boldsymbol{\nabla}\boldsymbol{u}\right) + \tfrac{1}{3}\left(\boldsymbol{\nabla}\rho + \boldsymbol{u}\frac{\partial\rho}{\partial\tau}\right) = \boldsymbol{J}\times\boldsymbol{B} + \boldsymbol{\nabla}\cdot(2\rho\nu\mathsf{S}), \tag{2.4}$$

$$\frac{\partial\rho}{\partial\tau} + \boldsymbol{\nabla}\cdot(\tfrac{4}{3}\rho\boldsymbol{u} - \kappa\boldsymbol{\nabla}\rho) = a\Gamma_\phi\rho_\phi + \boldsymbol{J}^2/\sigma_E + 2\rho\nu\mathsf{S}^2, \tag{2.5}$$

$$\frac{\mathrm{d}\ln a}{\mathrm{d}\tau} = \mathcal{H}, \tag{2.6}$$

where $\mathcal{H}$ is the comoving Hubble parameter, Γ_ϕ is the decay rate of the inflaton into photons, $\boldsymbol{J}$ is the current density, α is the axion coupling constant, f is the axion decay constant, ν is the viscosity, S is the rate-of-strain tensor with the components $\mathsf{S}_{ij} = (\partial_i u_j + \partial_j u_i)/2 - \delta_{ij}\partial_k u_k/3$, σ_E is the electric conductivity, and m_a is the axion mass. We solve these equations together with a constitutive relation for $\boldsymbol{J}$ through an Ohm's law and the axion potential $V(\phi)$, constraint equations for $\boldsymbol{E}$ and $\boldsymbol{B}$, and the Friedmann equation relating the comoving Hubble parameter $\mathcal{H}$ with the four energy densities in the Friedmann equation are [20]. Near the end of inflation, $V(\phi)$ is well approximated by a quadratic potential. Thus, we have

$$V(\phi) = \tfrac{1}{2}m_\mathrm{a}^2\phi^2, \tag{2.7}$$

$$\boldsymbol{J} = \sigma_E(\boldsymbol{E} + \boldsymbol{u}\times\boldsymbol{B}), \tag{2.8}$$

$$\boldsymbol{\nabla}\cdot\boldsymbol{E} = -\frac{\alpha}{f}\boldsymbol{B}\cdot\boldsymbol{\nabla}\phi, \quad \boldsymbol{\nabla}\cdot\boldsymbol{B} = 0, \tag{2.9}$$

$$\mathcal{H}^2 = \frac{8\pi}{3\,a^2}\langle\rho_\phi + \rho_E + \rho_B + \rho\rangle, \tag{2.10}$$

$$\tag{2.11}$$

where

$$\rho_\phi = \tfrac{1}{2}(\phi')^2 + \tfrac{1}{2}(\boldsymbol{\nabla}\phi)^2 + a^2V(\phi), \quad \rho_E = \boldsymbol{E}^2/2, \quad \text{and} \quad \rho_B = \boldsymbol{B}^2/2. \tag{2.12}$$

The mean radiation energy density ρ is given by equation (2.5). There is also the mean kinetic energy density,

$$\rho_\mathrm{kin} = \tfrac{2}{3}\rho\boldsymbol{u}^2, \tag{2.13}$$

but it does not constitute a separate entity in the Friedmann equation, because it is already included as part of ρ in the T^{00} component of the energy–momentum tensor; but see ref. [21] for subtleties regarding the 2/3 factor.

2.2 Flow of energy

The energy that leads to the establishment of a radiation-dominated universe with magnetic fields at the end of inflation comes from the inflaton field ϕ. The Chern-Simons coupling

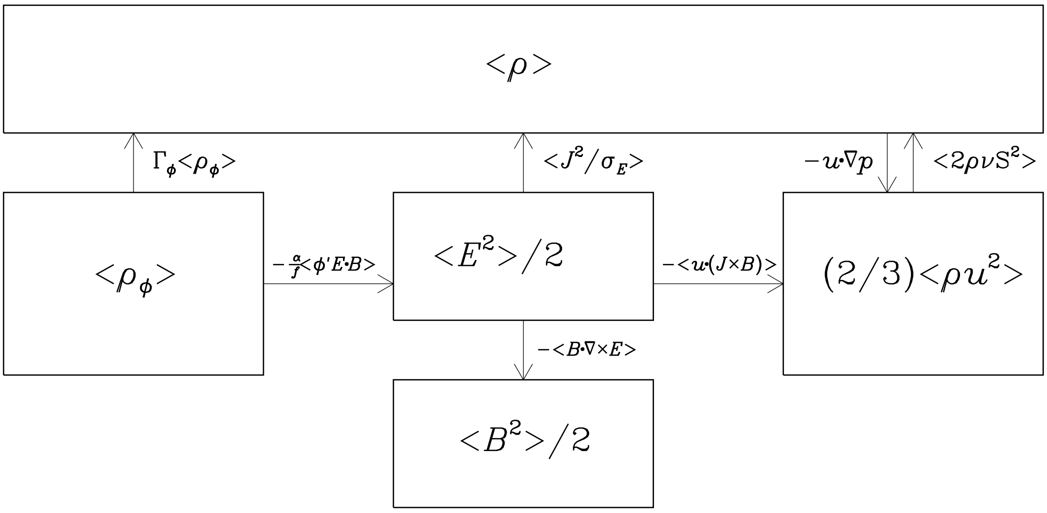

Figure 1. Flow of energy showing the sourcing of radiation energy density $\langle\rho\rangle$ through the decay of inflaton energy density $\langle\rho_\phi\rangle$, as well as the dissipation of electromagnetic and kinetic energy densities, $\langle\rho_E+\rho_B\rangle$ and $\langle\rho_{\rm kin}\rangle$, respectively.

$\propto \phi' F\tilde{F}$ with the electromagnetic field tensor F and its dual $\tilde{F}$, which is here the pseudoscalar ϕ, leads to an exponential growth of electric and magnetic fields. Those electromagnetic fields then also drive plasma motions. As alluded to in the introduction, the plasma motions are important for establishing an inverse cascade that leads to progressively larger length scales of the magnetic field. The development of large length scales of the magnetic field is an important property that is unique to MHD and is not found in purely hydrodynamic flows. Large length scales help seeding the growth of astrophysical magnetic fields. There are also lower and upper limits on such fields. Kiloparsec fields also facilitate their detectability using, for example, radio waves [22] and gamma rays [23]. The Schwinger current leads to resistive and viscous heatings, which provide an early source of radiation energy density.

At the end of inflation, the inflaton itself decays into radiation and provides an even stronger source of radiation energy density. All these processes are sketched in figure 1, where $\langle\rho_\phi\rangle$ is the comoving mean energy density of the inflaton, $-(\alpha/f)\,\langle\phi'\,\boldsymbol{B}\cdot\boldsymbol{E}\rangle$ is the source term of electromagnetic energy from the conformal time derivative of the inflaton, ϕ', $\langle\rho_E\rangle=\langle\boldsymbol{E}^2/2\rangle$ and $\langle\rho_B\rangle=\langle\boldsymbol{B}^2/2\rangle$ are the electric and magnetic energy densities that also exchange energies among themselves through the term $\langle\boldsymbol{B}\cdot\boldsymbol{\nabla}\times\boldsymbol{E}\rangle$ until the conductivity has become large enough and the magnetic energy density dominates over the electric energy density. Next, $\langle\rho_{\rm kin}\rangle=\frac{2}{3}\langle\rho\boldsymbol{u}^2\rangle$ is the mean kinetic energy density of an ultrarelativistic plasma, sourced by the work done by the Lorentz force, $\langle\boldsymbol{u}\cdot(\boldsymbol{J}\times\boldsymbol{B})\rangle$. Both kinetic and magnetic energies dissipate with the fluxes $\langle 2\nu\rho\mathbf{S}^2\rangle$ and $\langle\boldsymbol{J}^2/\sigma_E\rangle$ and contribute to reheating the universe. However, most of the reheating comes from the decay of the inflaton with the flux $(\alpha/f)\,\langle\phi'\,\boldsymbol{B}\cdot\boldsymbol{E}\rangle$.

In earlier work [19], the symbol ρ_χ has been used for all the electromagnetically dissipated energy, but part of this goes first into kinetic energy via the work done by the Lorentz force, $\langle\boldsymbol{u}\cdot(\boldsymbol{J}\times\boldsymbol{B})\rangle$, before being dissipated viscously, while the other part goes directly into radiation through resistive heating. In the MHD equations describing the radiation-dominated era of the universe, the radiation energy density $\rho_{\rm rad}$, which includes the rest-mass energy density of the plasma, is analogous to the usual gas density in MHD [10]. To avoid excessive use of the subscript "rad", and to facilitate the similarity with the usual MHD equations, we omit the subscript in the following and simply refer to it as ρ. Thus, we have $\rho_\chi = \rho + \rho_{\rm kin}$ for all the electromagnetically dissipated energy. The reason for the $2/3$ factor in the expression for the kinetic energy is related to the $4/3$ factor in equations (2.4) and (2.5); see ref. [21] for details.

2.3 Inflaton evolution and decay

Dotting equation (2.1) with ϕ', volume averaging, and integrating by parts, we obtain

$$\frac{d\langle\rho_\phi\rangle}{d\tau} + (2\mathcal{H} + a\Gamma_\phi)\langle\phi^2\rangle/2 = \frac{\alpha}{f}\langle\phi'\,\boldsymbol{E}\cdot\boldsymbol{B}\rangle/a^2, \tag{2.14}$$

We assume $\Gamma_\phi = 0$ prior to the end of inflation, which is marked by $d\mathcal{H}/d\tau = 0$. After that moment, we set $\Gamma_\phi = \Gamma_{\phi 0}$, where $\Gamma_{\phi 0}$ is taken to be an input parameter. By taking it to be larger than the theoretical value [24, 25], we can artificially reduce the transition time to a radiation dominated era.

Once the system begins to enter the radiation-dominated era, the oscillations of ϕ become progressively more rapid. This is because of the a^2 factor in front of the $V(\phi)$ term of the evolution equation for ϕ. Therefore, once the comoving value of the inflaton energy $a^4\rho_\phi$ drops below a certain critical value, we set $\phi = 0$ and omit its evolution equation from then onward.

Let us now discuss the momentum and continuity equations that describe turbulent flow and which also make the magnetic field turbulent. The nonrelativistic limit has been derived from the fully relativistic equations [10, 26]. The continuity equation for the comoving radiation and energy density ρ also includes source terms from the decay from the decay of the inflaton as well as resistive and viscous heatings.

2.4 Schwinger pair production

A crucial step in producing an MHD plasma from the vacuum left at the end of inflation is the emergence of an electric current density through the Schwinger effect. The $\boldsymbol{u}\times\boldsymbol{B}$ term results from the Lorentz boost to a rest frame. It corresponds to the electromotive force and leads to a feedback of the plasma velocity onto the electromagnetic field. For σ_E, we adopt the prescription of ref. [27] with

$$\sigma_E = \frac{(e|Q|)^3}{6\pi^2\mathcal{H}} B_{\rm rms} \coth\left(\frac{\pi B_{\rm rms}}{E_{\rm rms}}\right), \tag{2.15}$$

see also refs. [28–30] for earlier work. Here, e is the gauge coupling constant and Q is the particle's charge. In equation (2.15), the ratio $|\boldsymbol{B}|/|\boldsymbol{E}|$ is at early times between $1/2$ and 1, and later much larger than unity. However, because of the additional π factor, the $\coth(\pi|\boldsymbol{B}|/|\boldsymbol{E}|)$ factor is always approximately unity and can be omitted. Thus, we find that, to a good approximation, $\sigma_E \approx 0.004 \times |\boldsymbol{B}|/\mathcal{H}$ in our units. This prescription therefore corresponds to an Ohm's law with a conductivity that depends essentially only on $|\boldsymbol{B}|$ and $\mathcal{H}$. In particular, it does not depend on the axion mass or other parameters that we vary in this study. Furthermore, In earlier work, it was found in earlier work [19] that the results with spatially varying and spatially uniform prescriptions are rather similar. Therefore, we use in the following the prescription based on the rms values of $\boldsymbol{E}$ and $\boldsymbol{B}$.

2.5 Induction equation

To obey $\boldsymbol{\nabla} \cdot \boldsymbol{B} = 0$ at all times, we write equation (2.3) in terms of the magnetic vector potential $\boldsymbol{A}$ and solve the uncurled form of equation (2.3), which yields

$$\frac{\partial \boldsymbol{A}}{\partial \tau} = -\boldsymbol{E} + \boldsymbol{\nabla} A_0, \tag{2.16}$$

where $\boldsymbol{B} = \boldsymbol{\nabla} \times \boldsymbol{A}$. For reasons that we explain below, we use the resistive gauge [31],

$$A_0 = \sigma_E^{-1} \boldsymbol{\nabla} \cdot \boldsymbol{A}. \tag{2.17}$$

This formulation has the computational advantage that in the high conductivity limit, when the displacement current can be omitted, the uncurled induction equation attains a diffusion operator in the form proportional to $\nabla^2 \boldsymbol{A}$.

Inserting equation (2.8) into equation (2.2) and solving for $\boldsymbol{E}$, we have

$$\frac{\partial \boldsymbol{E}}{\partial \tau} + \sigma_E \boldsymbol{E} + \frac{\alpha}{f} \boldsymbol{\nabla} \phi \times \boldsymbol{E} = \boldsymbol{\nabla} \times \boldsymbol{B} - \sigma_E \boldsymbol{u} \times \boldsymbol{B} - \frac{\alpha}{f} \dot{\phi} \boldsymbol{B}. \tag{2.18}$$

The operator on the left-hand side can we written in matrix form as

$$-\mathsf{M} \boldsymbol{E} = \boldsymbol{u} \times \boldsymbol{B} + \sigma_E^{-1} \left(\frac{\alpha}{f} \phi' \boldsymbol{B} - \boldsymbol{\nabla} \times \boldsymbol{B} \right), \tag{2.19}$$

which has the components

$$\mathsf{M}_{ij} = \left(1 + \sigma_E^{-1} \partial / \partial \tau\right) \delta_{ij} - \epsilon_{ijk} \Lambda_k \tag{2.20}$$

with $\boldsymbol{\Lambda} = \sigma_E^{-1} (\alpha / f) \, \boldsymbol{\nabla} \phi$ being a vector with the components λ_k, where $k = 1$, 2, and 3 are the three spatial components. It is then also convenient to define a temporal component as $\Lambda_0 = \sigma_E^{-1} (\alpha / f) \, \phi'$, so that we can write equation (2.16) in the form

$$\frac{\partial \boldsymbol{A}}{\partial \tau} = \boldsymbol{u} \times \boldsymbol{B} + \Lambda_0 \boldsymbol{B} + \sigma_E^{-1} \nabla^2 \mathbf{A} + \boldsymbol{R}, \tag{2.21}$$

where

$$\boldsymbol{R} = \boldsymbol{\Delta} \left(\boldsymbol{u} \times \boldsymbol{B} + \Lambda_0 \boldsymbol{B} - \sigma_E^{-1} \boldsymbol{\nabla} \times \boldsymbol{B} \right) + \sigma_E^{-1} \frac{\partial \boldsymbol{E}}{\partial \tau} \tag{2.22}$$

is a rest term, $\boldsymbol{\Delta}$ is a matrix with the components $\Delta_{ij} = \epsilon_{ijk} \Lambda_k$. The minus sign on the left-hand side of equation (2.19) has been applied in view of equation (2.16) and its role as induction equation in MHD. The present form with the time derivative in M will be useful in connection with magnetic helicity considerations.

2.6 Relevance of the displacement current

When the conductivity is large, the displacement current, and therefore the time derivative in M, can be neglected. This is the case well after the end of inflation, when $\boldsymbol{J}$ has become important. This is what we refer to as the strict MHD limit. In that case, the Ampère equation for $\boldsymbol{J}$ can be written in the form

$$\boldsymbol{J} = \boldsymbol{\nabla} \times \boldsymbol{B} - \frac{\alpha}{f} \left(\frac{\partial \phi}{\partial \tau} \boldsymbol{B} + \boldsymbol{\nabla} \phi \times \boldsymbol{E} \right). \tag{2.23}$$

Note, however, that this equation cannot be used as a prognostic equation, because it contains the unknown $\boldsymbol{E}$ on the right-hand side. Therefore, we have to work with the inverse of M, which has the components

$$\left(\mathsf{M}^{-1}\right)_{ij} = \left(\delta_{ij} + \epsilon_{ijk}\,\Lambda_k + \Lambda_i\Lambda_j\right) / \det\mathsf{M}, \tag{2.24}$$

where $\det\mathsf{M} = 1 + (\boldsymbol{\nabla}\tilde{\phi})^2$ is the determinant of M. The induction equation can then be written as

$$\frac{\partial\mathbf{A}}{\partial\tau} = \mathsf{M}^{-1}\left(\boldsymbol{u}\times\boldsymbol{B} + \Lambda_0\boldsymbol{B} - \sigma_E^{-1}\boldsymbol{\nabla}\times\boldsymbol{B}\right). \tag{2.25}$$

Equation (2.25) is similar to the induction equation with the chiral magnetic effect included [32], and also similar to the induction equation in mean-field electrodynamics, where the term $\tilde{\phi}'$ acts as an α effect; see [33] for a more detailed comparison between those two. It turns out that we can seamlessly switch from solving the combined equations (2.2) and (2.3) to solving just equation (2.25) when σ_E is large enough.

2.7 Model parameters

A crucial input parameter of a model is the inflaton mass m_a. Here we compare our three runs with In the present work, we vary the value of m_a between 10^{-7} and 10^{-5}. We note, however, that there are tight upper limits on the value of m_a.

The conductivity, as given by equation (2.15), can reach large values at late times. This leads to the development of turbulence where magnetic dissipation occurs at very small length scales that cannot be resolved with the limited number of mesh points.

For the viscosity, we fix the value of the magnetic Prandtl number, $\mathrm{Pr_M} = \nu\sigma_E$. For all our runs, we choose the values $\mathrm{Pr_M} = 1$, 10, and 100. Likewise, we quantify the radiative diffusivity κ in terms of the Schmidt number, $\mathrm{Sc} = \nu/\kappa$.

2.8 Diagnostic quantities

Important insight into the evolution of the system is provided by time series of ρ_ϕ, ρ_E, ρ_B, ρ, and ρ_kin. We always show them as comoving quantities. We also study comoving energy spectra. We define the spectrum of a scalar quantity $v(\boldsymbol{x})$ as

$$\mathrm{Sp}(v(\boldsymbol{x})) = \oint |\tilde{v}(\boldsymbol{k})|^2\, k^2\, d\Omega_k, \tag{2.26}$$

where Ω_k is the solid angle in $\boldsymbol{k}$ space, denoted by a tilde. The spectrum of a vectorial quantity as given by the sum of the spectra of it components. The comoving energy spectrum of the inflaton is then given as

$$E_\phi(k,\tau) = \tfrac{1}{2}a^2\,\left[\mathrm{Sp}(\phi') + \mathrm{Sp}(\boldsymbol{\nabla}\phi) + a^2 m_\mathrm{a}\mathrm{Sp}(\phi)\right], \tag{2.27}$$

while the electric, magnetic, and kinetic energy spectra are given as

$$E_E(k,\tau) = \tfrac{1}{2}\mathrm{Sp}(\boldsymbol{E}), \quad E_B(k,\tau) = \tfrac{1}{2}\mathrm{Sp}(\boldsymbol{B}), \quad \text{and} \quad E_\mathrm{kin}(k,\tau) = \tfrac{2}{3}\langle\rho\rangle\mathrm{Sp}(\boldsymbol{u}). \tag{2.28}$$

They obey $\int E_\phi(k,\tau)\,dk = \langle\rho_\phi\rangle$, $\int E_E(k,\tau)\,dk = \langle\rho_E\rangle$, $\int E_B(k,\tau)\,dk = \langle\rho_B\rangle$, and $\int E_\mathrm{kin}(k,\tau)\,dk = \langle\rho_\mathrm{kin}\rangle$. We also present the radiation energy variance spectrum as

$$E_\rho(k,\tau) = [\langle\rho\rangle/\langle\rho^2\rangle]\,\mathrm{Sp}(\rho), \tag{2.29}$$

which is thus normalized to obey $\int E_\rho(k,\tau)\,dk = \langle\rho\rangle$.

In some cases, we also define helicity-like spectra. They are based on the product (or dot product) of two quantities (u and v, say) and are written as

$$\mathrm{Sp}(u(\boldsymbol{x}), v(\boldsymbol{x})) = \mathrm{Re} \oint \tilde{u}^*(\boldsymbol{k})\tilde{v}(\boldsymbol{k})\, k^2\, d\Omega_k, \tag{2.30}$$

Similarly to the energy spectra, they obey $\int \mathrm{Sp}(u,v)\,dk = \langle uv\rangle$.

We characterize the resulting magnetic field by its integral scale defined as

$$\xi_\mathrm{M} = \int k^{-1} E_B(k,\tau)\,dk \bigg/ \int k^{-1} E_B(k,\tau)\,dk, \tag{2.31}$$

and the (nonrelativistic) Alfvén velocity $v_\mathrm{A} = B_\mathrm{rms}/\sqrt{(4/3)\rho}$, based in the rms magnetic field. The level of turbulence is quantified by the Reynolds and Lundquist numbers,

$$\mathrm{Re} = u_\mathrm{rms}\xi_\mathrm{M}/\nu, \quad \mathrm{Lu} = v_\mathrm{A}\xi_\mathrm{M}/\sigma_E, \tag{2.32}$$

respectively.

We often present our results in terms of the number of e-folds of a after the end of inflation. It is related given by the logarithm of $a(\tau)$ and denoted as $N = \ln a - \ln a_\mathrm{end}$, where $\ln a_\mathrm{end}$ is the value where $\mathcal{H}$ is maximum. For our runs with $\phi_0 = 0.7$, we have $\ln a_\mathrm{end} \approx 3.17$. This value is independent of the value of m_a. Alternatively, we give the value of τm_a and find that certain aspects of the results depend only mildly on the value of m_a.

2.9 Initial conditions

Following earlier work [19], we choose our initial conformal time to be $\tau_0 = -\mathcal{H}^{-1}$, where $a(\tau_0) = 1$ and $H(\tau_0) = (8\pi/3)\,V(\phi_0)\,a^2$ with ϕ_0 being the initial value of ϕ. As in earlier work, we choose $\phi_0 = 0.7$, which is appropriate for values of α/f below 90.

To compare models with different values of m_a, we must adjust the size of the domain correspondingly. Thus, the lowest wave number of the domain is chosen to be $k_1 = 0.1\,m_\mathrm{a}$ and the initial position of spectral peak is taken to be $k_\mathrm{p} = 50\,m_\mathrm{a}$. We also choose the value of Γ_ϕ to be a certain fraction of m_a and take $\Gamma_\phi = 10^{-3}\,m_\mathrm{a}$. Finally, for numerical reasons, to avoid initially infinite accelerations we limit the initial nominal value of $B_\mathrm{rms}/\sqrt{\rho}$ by beginning our simulations with a finite initial value of $\rho = \rho_0$. Since the magnetic and electric field strengths scale quadratically with m_a, and ρ scales with the fourth power of m_a^4, and the initial value of ρ is chosen to be $\rho_0 = (0.1\,m_\mathrm{a})^4 = 10^{-4}\,m_\mathrm{a}^4$. Thus, in practice, we use $\rho_0 = 10^{-24}$ for $m_\mathrm{a} = 10^{-5}$, $\rho_0 = 10^{-28}$ for $m_\mathrm{a} = 10^{-6}$, and $\rho_0 = 10^{-32}$ for $m_\mathrm{a} = 10^{-7}$.

2.10 Numerical aspects

We solve our system of equations with the Pencil Code [34], where all options for an efficient solution of the axion inflation with subsequent MHD evolution have been included in its latest version[1]. In particular, there are the options to turn on inflaton decay at the end of inflation, τ_end through a step function with an additional $f(a)$ factor for a smooth transition,

$$\Gamma_\phi(N) = \Gamma_{\phi 0}\Theta_{\Delta N}(N - N_\mathrm{end}), \tag{2.33}$$

[1] https://github.com/pencil-code/pencil-code/

where $\Gamma_{\phi 0}$ is considered a free parameter, for which we study different values, independently of the theoretical value of refs. [24, 25], which also scales differently with $m_{\rm a}$. Here, we consider values in the range $10^{-8} \leq \Gamma_{\phi 0} \leq 10^{-11}$ and focus on the combinations $\Gamma_{\phi 0}/m_{\rm a} = 10^{-3}$ and 10^{-4}. It turns our that for small axion mass ($m_{\rm a} = 10^{-7}$), a sudden jump in equation (2.33) leads to numerical problems at $N = N_{\rm end}$. We therefore smoothen the transition such that the logarithm of $\Gamma_\phi(N)$ varies linearly between a certain fraction (typically 10^{-4}) of $\Gamma_{\phi 0}$ within the interval ΔN.

At the end of reheating, which we determine through the condition $\rho_\phi < \rho_\phi^{\rm min}$ with an assumed minimal comoving energy density of the inflaton, $\rho_\phi^{\rm min}$, we terminate the integration of ϕ and set $\phi = 0$ after that time. This alleviates the progressively more restrictive time step constraint from the rapid inflaton oscillations.

We also choose a certain time, after which the displacement current is neglected. In practice, we choose this time to be $N = 2$, i.e., two e-folds of a after the end of inflation. This alleviates the time step constraint for high conductivities, $\delta t < \sigma_E^{-1}$, when the displacement current is still included. In practice, however, the times step constraint from ϕ is more constraining and becomes even shorter until the end of reheating. There are a number of other time step constraints. One of them is the Courant-Friedrich-Levy condition based on the speed of light (which is unity), so $\delta t \leq \delta x$.

There are two more time step constraints. One of them results from the viscosity ν and the radiative diffusivity κ, namely

$$\delta\tau < C_{\rm diff}\delta x^2/\max(\nu,\kappa). \tag{2.34}$$

In the MHD regime, also the magnetic diffusivity σ_E^{-1} imposes a similar constraint. Finally, there is a constraint from the axion mass, i.e., $\delta\tau < C_0 m_{\rm a}$. Thus, in summary, we have

$$\delta\tau < \min\left(C_{\rm diff}\delta x^2/\max(\nu,\kappa), ...\right). \tag{2.35}$$

3 Results

3.1 Evolution of energy densities

We begin by inspecting the evolution of the five energy reservoirs, $\langle\rho_\phi\rangle$, $\langle\rho_E\rangle$, $\langle\rho_B\rangle$, $\langle\rho_{\rm kin}\rangle$, and $\langle\rho\rangle$. The case of a large axion mass is in some ways easier to understand and there are fewer special effects that require discussion. This is probably related to the fact that in that case, the energy densities of the different reservoirs entering in equation (2.10) are of similar order of magnitude. We begin with the case with $m_{\rm a} = 10^{-5}$ and $\Gamma_\phi = 10^{-8}$; see figure 2. In the beginning, the largest energy reservoir is $\langle\rho_\phi\rangle$. It is responsible for driving $\mathcal{H}^2$ itself, such that equation (2.10) is obeyed.

As we have seen in section 2.2, the displacement current only plays a role during inflation when it mediates the energy transfer from the axions field to the magnetic field. Before the end of inflation, the electric energy gains from the axion term, $(\alpha/f)\langle\phi'\boldsymbol{B}\cdot\boldsymbol{E}\rangle$, but suffer losses from $\langle\boldsymbol{B}\cdot\boldsymbol{\nabla}\times\boldsymbol{B}\rangle$. Those losses directly feed the magnetic energy. Since Schwinger currents are still negligible, the $\langle\boldsymbol{J}\cdot\boldsymbol{E}\rangle$ term is still small.

Just after the end of inflation, the electric energy reaches a maximum and then declines; see figure 3. By that time, the electric energy has sourced the magnetic field, and it has also at the same time led to heating via the $\langle\boldsymbol{J}^2/\sigma_E\rangle$ term and to driving kinetic energy through the $\langle\boldsymbol{u}\cdot(\boldsymbol{J}\times\boldsymbol{B})\rangle$ term.

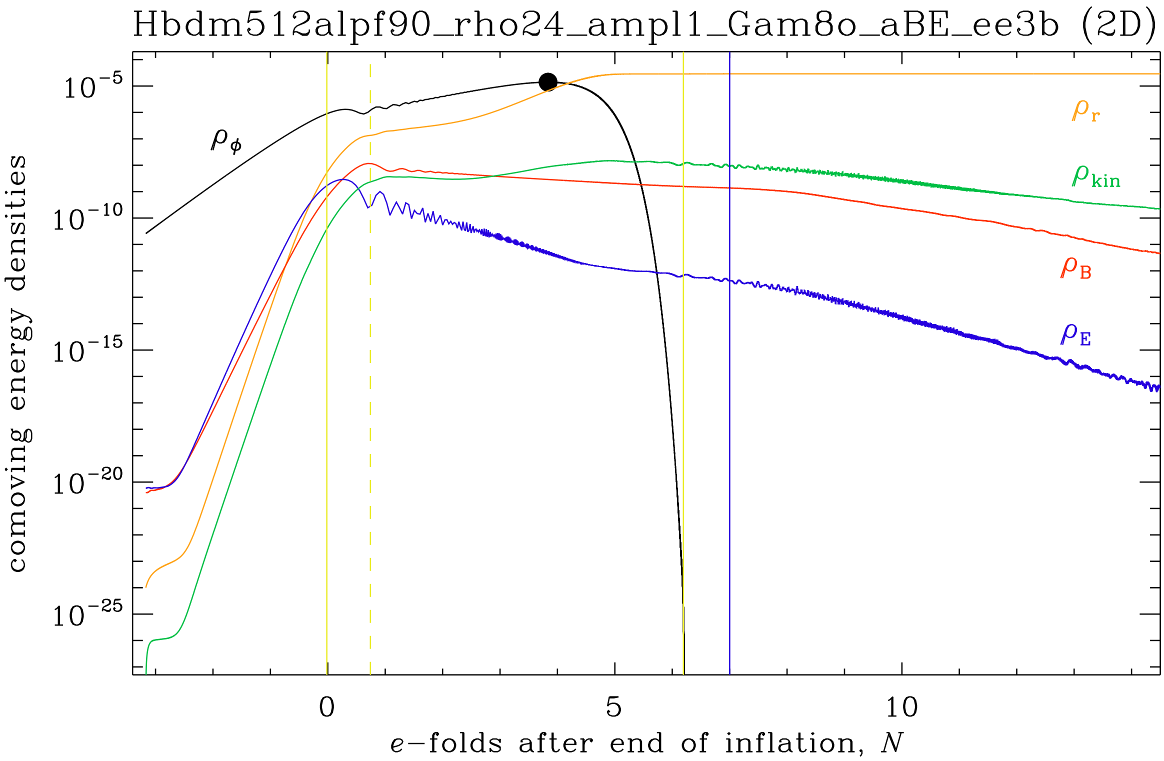

Figure 2. Evolution of the five energy density in the model with $m_{\rm a} = 10^{-5}$. The yellow vertical lines mark the end of inflation and the reheating interval. The blue vertical lines marks the beginning of the MHD evolution without displacement current.

We see from figure 3 that heating is rather efficient before the end of inflation and lead to a rapid growth with $\langle\rho\rangle \propto \exp(5N)$. This is true for all three values of $m_{\rm a}$. Note that the mean kinetic energy density growth at about the same rate. Clearly, $\langle\rho\rangle$ cannot be sourced by the axion field, so it can only grow because of the $\boldsymbol{J}^2/\sigma_E$ heating term. This changes only for $N > 0$ when ρ can also grow because of the $a\Gamma_\phi\langle\rho_\phi\rangle$ term. When that happens, $\rho_{\rm kin}$ continues to grow, but then the contribution from $W_{\rm L}$ has diminished, so it can only grow because of radiative pressure driving through the term $\boldsymbol{u}\cdot\boldsymbol{\nabla}p$. This obviously requires nonuniformities of ρ, which can only be caused by the heating terms $\boldsymbol{J}^2/\sigma_E$ and $2\nu\rho\mathbf{S}^2$. To quantify this, we monitor the departures from the average through $\langle\rho^2\rangle/\langle\rho\rangle^2 - 1$. The can also be seen from the $E_\rho(k)$ spectra in figure 8.

Interestingly, the $E_\rho(k)$ and $E_{\rm kin}(k)$ spectra have similar shapes at different times. This suggests that there is indeed a strong coupling between ρ and $\rho_{\rm kin}$ energy reservoirs, and that $\rho_{\rm kin}$ can indeed be driven through ρ from ρ_ϕ. The uniformity of the axion field is almost entirely driven by fluctuation in $\boldsymbol{B}\cdot\boldsymbol{E}$. This will be discussed next.

3.2 Driving gradients in ρ

The generation of gradients in ρ is significant, because ρ gradients can drive kinetic energy. As alluded to above, the ρ gradients can be driven by ρ_ϕ gradients, which, in turn, are driven by fluctuations in $\boldsymbol{B}\cdot\boldsymbol{E}$. Since the energy in the ϕ field is much larger than that in $\boldsymbol{E}$ and $\boldsymbol{B}$, it is possible that there might be some amplification process through the ϕ field.

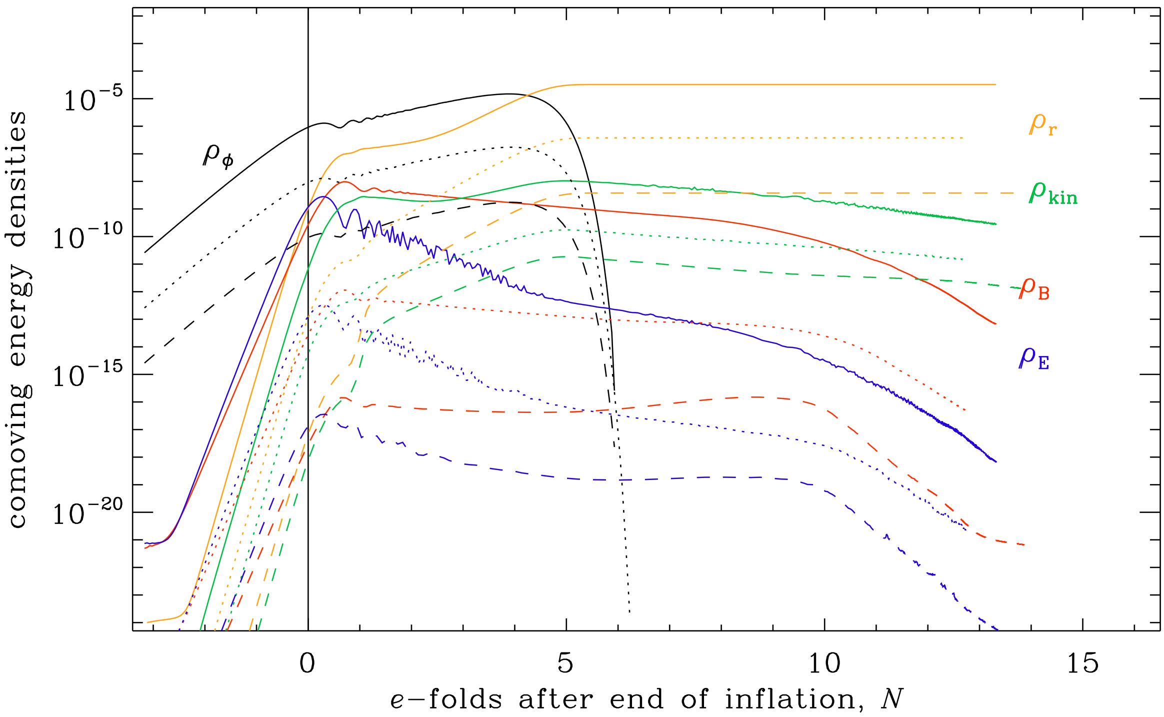

Figure 3. Evolution of the five energy densities in the model with $m_{\rm a} = 10^{-5}$, 10^{-6}, and 10^{-7}.

Note that the number of e-folds after the end of reheating is the same when Γ_ϕ scales with $m_{\rm a}$. Specifically, we find that the end occurs for $N \approx 6$ when $\Gamma_\phi = 10^{-3}\, m_{\rm a}$ and for $N \approx 7$ when $\Gamma_\phi = 10^{-4}\, m_{\rm a}$. Therefore, also the Lundquist number increases. Eventually, Lu exceeds the maximum value possible for a given resolution and we can no longer trust the simulation.

In figure 14, we compare Run C with our usual value $\mathrm{Pr_M} = 10$ with one where $\mathrm{Pr_M} = 1$. For $\mathrm{Pr_M} = 1$, we expect the kinetic energy dissipation to be lower. This can either lead to a pile-up of kinetic energy or perhaps also to a reduced energy uptake by kinetic energy and thereby to a larger electromagnetic energy. It turns out that the former is true, i.e., there is a pile-up of kinetic energy owing to the reduced dissipation, and also a somewhat less pronounced pile-up of magnetic fields.

3.3 Dependence on the axion mass

There is an interesting mismatch between the scaling of axion energy density, and radiation energy density. While $\langle \rho_\phi \rangle$ is quadratic in $m_{\rm a}$, ρ_B and ρ_B are quartic in $m_{\rm a}$. The reason for the former is evident from equation X.

Figure 4 shows that ρ_ϕ scales with $m_{\rm a}^2$, while ρ scales with $m_{\rm a}^4$. Interestingly, also $\rho_{\rm kin}$ is found to scale with $m_{\rm a}^2$, while ρ_B and ρ_E scale with $m_{\rm a}^4$; see figure 4, where we study the scaling of the maxima of the various comoving energy densities with $m_{\rm a}$. Another important constraint arises from the finite size of the computational domain. This limits the scale of the magnetic field.

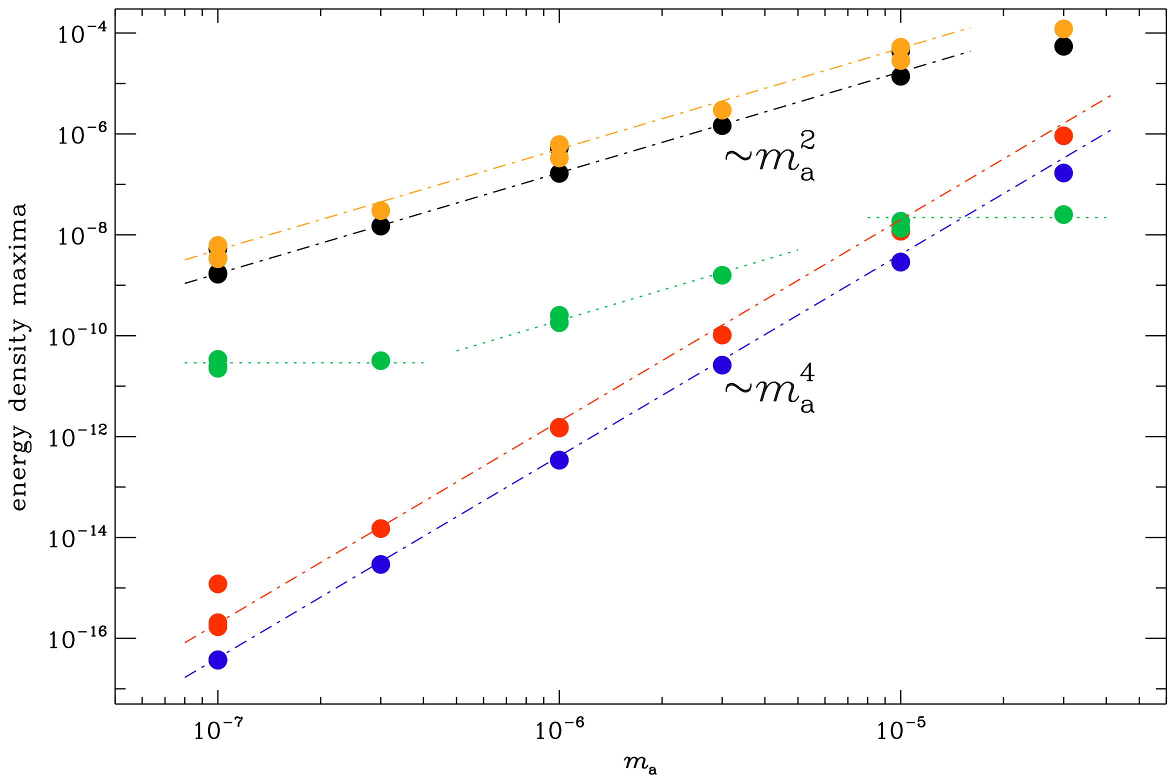

Figure 4. Dependence of the maxima of the different energy densities as a function of m_a.

Figure 5. Visualizations of $J_z(x, y, \tau)$ for different values of m_a and $m_a\tau$ for Runs A (top row), C (middle row), and E (bottom row). [**AB**: to add color bar.]

3.4 Late magnetic uprise for small axion mass

Comparing the magnetic field evolution for different values of m_a in figure 3, we see that the kinetic energy always exceeds the magnetic energy. However, for a small value of m_a, this difference increases. On the other hand, the magnetic energy now shows an increase toward late times. This is a consequence of the work done against the Lorentz force.

An increased value of σ_E reduces the resistive dissipation and, therefore, allows ρ_B to increase due to the continued work done against the Lorentz force.

3.5 Formation of coherent turbulence structures

At the end of inflation, the conductivity is already high enough to produce bulk motions well before the end of reheating and the beginning of the actual radiation-dominated era. This leads to turbulent motions, as can be seen from visualizations of J_z; see figure 5. Here we compare our three runs with $m_a = 10^{-7}$ (Run A), 10^{-6} (Run C), and 10^{-5} (Run E). Comparing Runs A and C, the images for times $m_a\tau = 1$ look similar, but the the result for Run A at $m_a\tau = 10$ looks more similar to that for Run C at $m_a\tau = 100$.

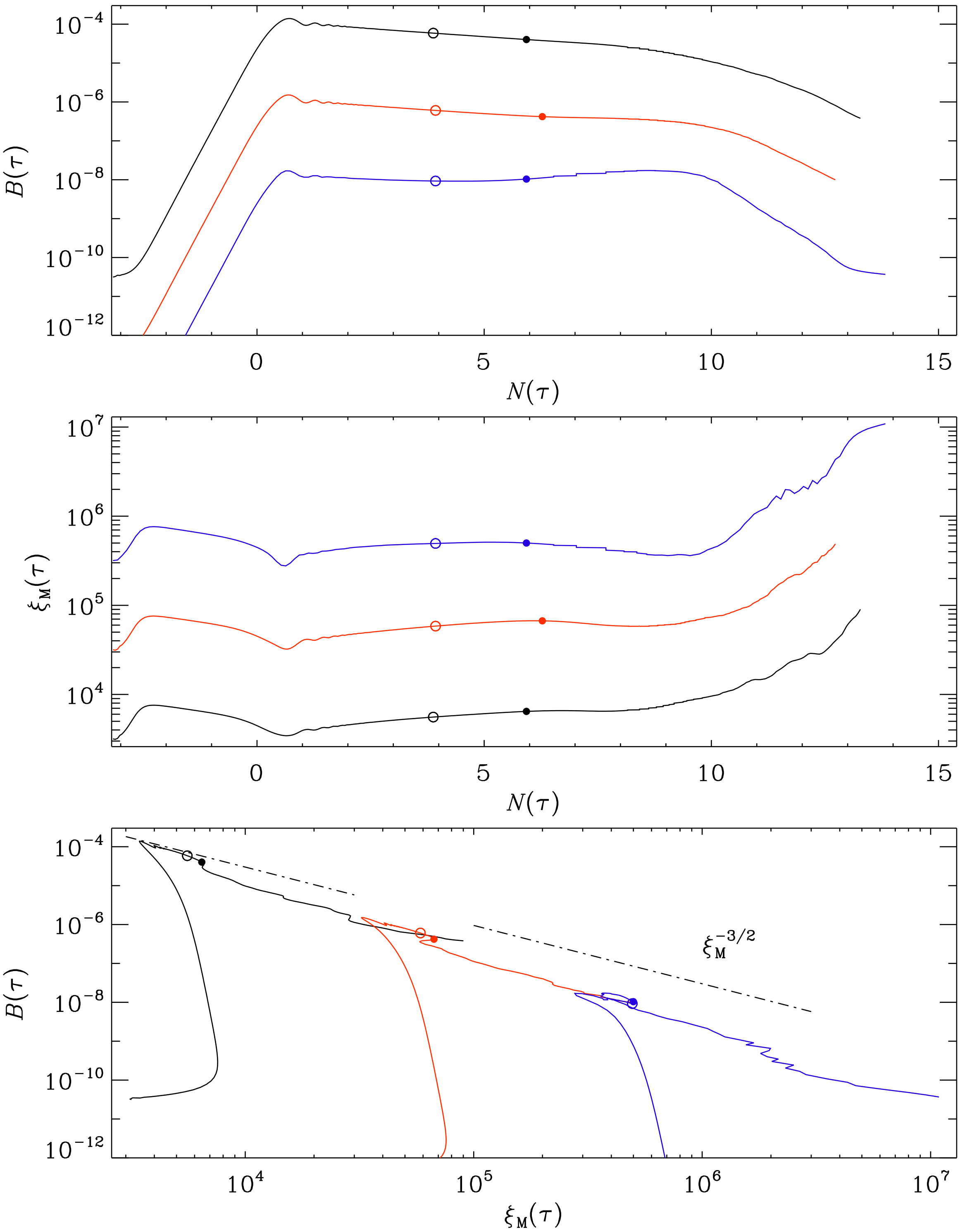

Figure 6. Parametric representations of $B(\tau)$, $\xi_{\rm M}(\tau)$, and $B(\tau)$ vs. $\xi_{\rm M}(\tau)$. The filled symbol marks the end of reheating.

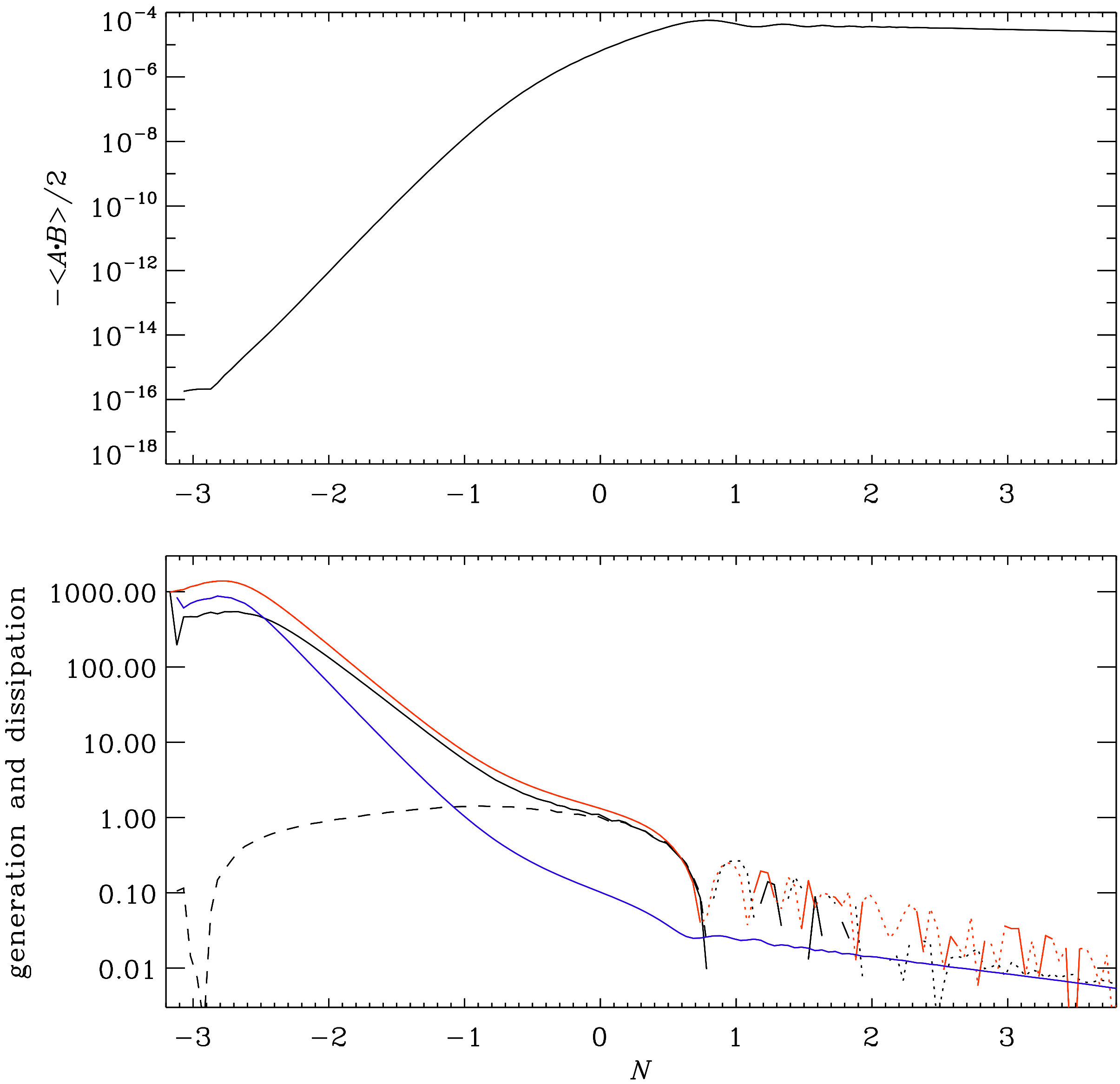

Figure 7. Magnetic helicity evolution and balance between generation and dissipation terms for Run C. Top: $-\langle \mathbf{A} \cdot \boldsymbol{B} \rangle/2$, bottom: sum of $[d\langle \boldsymbol{B} \cdot (\partial(\boldsymbol{A} + \boldsymbol{E})/d\tau\rangle]/B_{\mathrm{rms}}^2$ (solid black), just $[d\langle \mathbf{A} \cdot \boldsymbol{B} \rangle/d\tau]/B_{\mathrm{rms}}^2$ (dashed black), the red line shows $-(\alpha/f)\, \langle \phi' \boldsymbol{B}^2 \rangle/B_{\mathrm{rms}}^2$, and the blue line shows $-\sigma_E^{-1}\, \langle \boldsymbol{B} \cdot \boldsymbol{\nabla} \times \boldsymbol{B} \rangle/B_{\mathrm{rms}}^2$.

3.6 Spectral evolution

3.7 Evolution of the magnetic length scale

3.8 Dependence on Γ_ϕ

At early times, before the end of inflation, $\mathcal{H}$ increases and the comoving horizon scale decreases. After the end of inflation, the growth of $a(\tau)$ slow down and $\mathcal{H}^{-1}(\tau)$ increases $\propto a^{1/2}$, which is during the reheating era, and later $\propto a(\tau)$, when the universe has become radiation dominated. In figure 9, we compare the evolution of the comoving Hubble scale for different

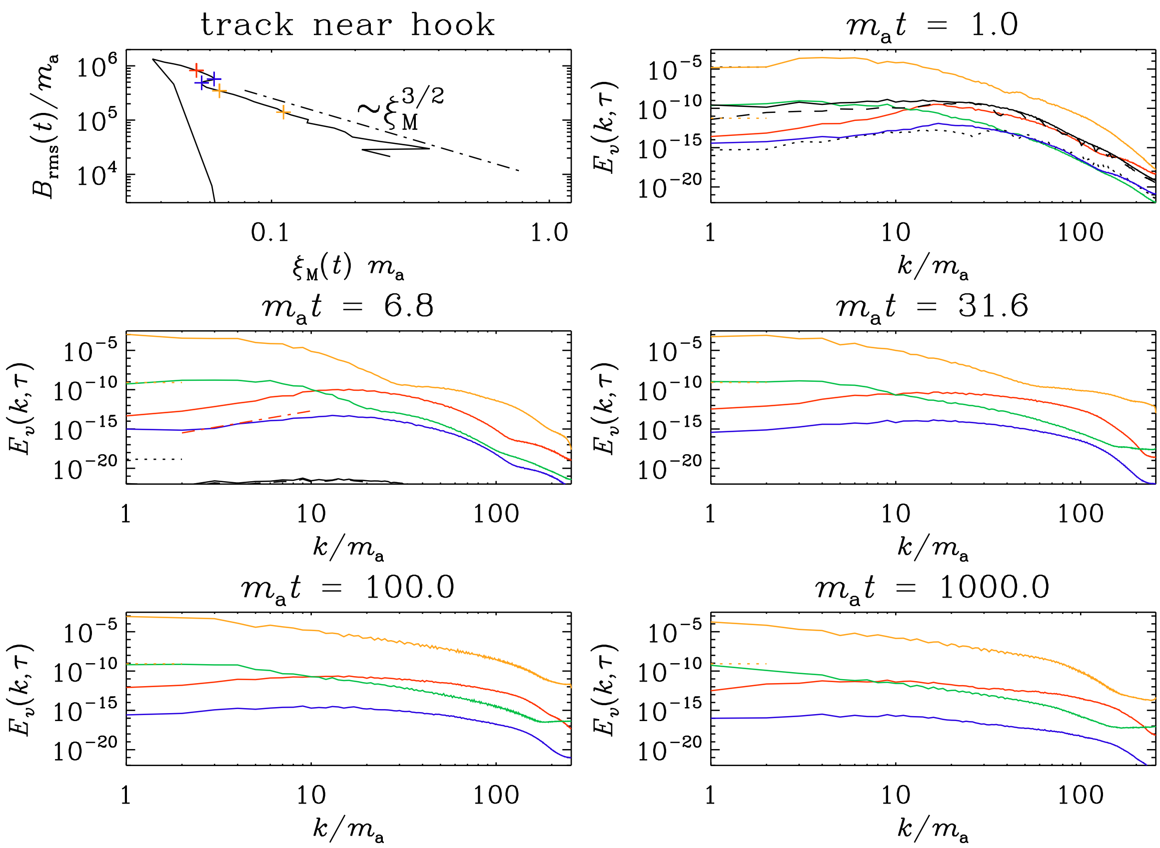

Figure 8. Diagnostic $B_{\rm rms}(\tau)$ vs. $\xi_{\rm M}(\tau)$ diagram (upper left) for Run A, along with spectra at the five times marked in the diagnostic diagram with + signs for the same run as in figure 2. The first three spectra show the decline of the inflaton field and the gradual built-up of an inertial range in the magnetic energy spectrum (red), corresponding to the passage of the hook. At the last two times, the peak of the spectrum moves further to toward low k. The subinertial range slope then becomes shallower due to the finite length of the subinertial range available.

values of Γ_ϕ and $m_{\rm a}$. Not surprisingly, a smaller value of Γ_ϕ prolongs the reheating phase; compare Runs A and B, and likewise Runs C and D. Note, however, that both Runs A and C have the same duration of reheating, and so do Runs B and D, confirming that the duration of reheating, $\Delta\tau_{\rm reh}$, scales with $m_{\rm a}^{-1}$. More specifically, we find that $\Delta\tau_{\rm reh}\, m_{\rm a}\, (\Gamma_\phi/m_{\rm a})^{1/3} \approx 0.6$–$0.8$; see table 1.

3.8.1 Implications of a modified scaling of Γ_ϕ with $m_{\rm a}$

In our present work, we focused on a linear scaling of Γ_ϕ with $m_{\rm a}$. This is motivated by the idea that we want to prevent the heating epoch to be too long in our model. This is particularly important because of the time step constraint imposed by solving for ϕ.

Using the expression of refs. [24, 25] implies that Γ_ϕ would be smaller than our present value of $10^{-4} m_{\rm a}$ by another factor of $m_{\rm a}\alpha/8f)^2 \approx (12.5\, m_{\rm a}\alpha/f)^2 \approx 10^{-8}$ for $m_{\rm a} = 10^{-7}$. A ten times smaller value of Γ_ϕ prolongs to reheating phase by around $\Delta N \approx 1$; see also table 1.

Empirically, we find that the reheating time is well approximated by the empirical expression $\Delta\tau_{\rm reh}\, m_{\rm a}\, (\Gamma_\phi/m_{\rm a})^{1/3} \approx 0.6$–$0.8$. Thus, if we insert the theoretical scaling, we see

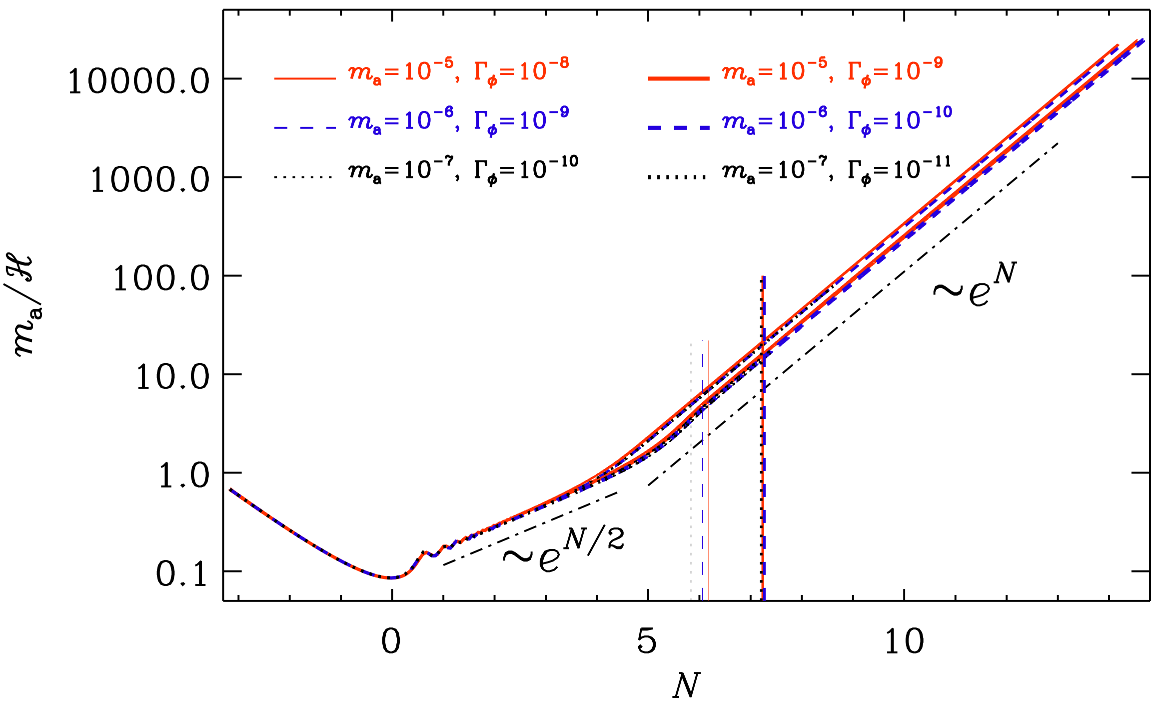

Figure 9. Comparison of $m_\mathrm{a}/\mathcal{H}$ for Runs A and B with $m_\mathrm{a} = 10^{-5}$ with $\Gamma_\phi = 10^{-8}$ (thin solid red) and $\Gamma_\phi = 10^{-9}$ (thick solid red), respectively, Runs C and D with $m_\mathrm{a} = 10^{-6}$ with $\Gamma_\phi = 10^{-9}$ (thin dashed blue) and $\Gamma_\phi = 10^{-10}$ (thick dashed blue), respectively, and Run E with $m_\mathrm{a} = 10^{-7}$ with $\Gamma_\phi = 10^{-11}$ (thin dashed black). The corresponding vertical lines mark the end of reheating.

that ... becomes... Specifically, we find that ...

3.9 Changes in the electromagnetic energy balance

By taking the product of equation (2.2) with $\boldsymbol{E}$, and of equation (2.3) with $\boldsymbol{B}$, adding the two equations, and averaging over our periodic volume, we obtain the equation for the electromagnetic energy balance,

$$\frac{\mathrm{d}}{\mathrm{d}\tau}\frac{\langle \boldsymbol{E}^2 + \boldsymbol{B}^2\rangle}{2} = -\frac{\alpha}{f}\langle \phi' \boldsymbol{B}\cdot\boldsymbol{E}\rangle - \langle \boldsymbol{J}^2/\sigma_E\rangle - \langle \boldsymbol{u}\cdot(\boldsymbol{J}\times\boldsymbol{B})\rangle. \tag{3.1}$$

Table 1. Duration of reheating for different combinations of m_a and Γ_ϕ.

Run	m_a	Γ_ϕ	N_reh	$\Delta\tau_\mathrm{reh}$	$\Delta\tau_\mathrm{reh}\, m_\mathrm{a}$	$\Delta\tau_\mathrm{reh}\, m_\mathrm{a}\,(\Gamma_\phi/m_\mathrm{a})^{1/3}$
A	10^{-5}	10^{-8}	6.2	8.1×10^5	8.1	0.81
B	10^{-5}	10^{-9}	7.2	1.7×10^6	16.5	0.77
C	10^{-6}	10^{-9}	6.1	6.7×10^6	6.7	0.67
D	10^{-6}	10^{-10}	7.3	1.6×10^7	15.7	0.73
E	10^{-7}	10^{-10}	5.8	5.5×10^7	5.5	0.55
F	10^{-7}	10^{-11}	7.2	1.5×10^8	14.8	0.69

In figure 10, we compare the conformal time to derivative of $\langle \boldsymbol{E}^2+\boldsymbol{B}^2\rangle/2$ with the three terms on the right-hand side of equation (3.1). We see that, during inflation, the electromagnetic energy increases, and its time derivative is essentially balanced by the axion term. During the reheating phase, the electromagnetic energy changes very little, but the axion term is still strong and is now balanced by dissipation $\langle \boldsymbol{J}^2/\sigma_E\rangle$. Some of the energy also goes into kinetic energy via the work done by the Lorentz force, $\langle \boldsymbol{u}\cdot(\boldsymbol{J}\times\boldsymbol{B})\rangle$. Finally, at the end of the reheating phase, there is no longer energy input from the axion field and the electromagnetic energy can only decay. Thus, we have a balance between the time derivative of the electromagnetic energy and the dissipation as well as work done by the Lorentz force.

Near the end of inflation, the growth of $\rho_{\rm EM}$ is entirely balanced by $-\frac{\alpha}{f}\langle\phi'\boldsymbol{B}\cdot\boldsymbol{E}\rangle$. It reaches a maximum at $N\approx 0.4$, when ρ_E and ρ_B are about equal and their sum balances $\mathrm{d}\rho_{\rm EM}/\mathrm{d}\tau$. [**AB**: This does not make sense sign wise. Expect $\mathrm{d}\rho_{\rm EM}/\mathrm{d}\tau=0$ at $N=0.4$.]

After that time, $\mathrm{d}\rho_{\rm EM}/\mathrm{d}\tau$ is mostly negative, while $-\frac{\alpha}{f}\langle\phi'\boldsymbol{B}\cdot\boldsymbol{E}\rangle$ and $\langle \boldsymbol{J}^2/\sigma_E\rangle$ display a slow oscillatory decay and are mostly in phase. This remains true until the end of reheating, when $-\frac{\alpha}{f}\langle\phi'\boldsymbol{B}\cdot\boldsymbol{E}\rangle$ drops rapidly to zero, and $W_{\rm L}$ and $Q_{\rm M}$ either approach each other (for other large values of $m_{\rm a}$) or $W_{\rm L}$ even exceeds $Q_{\rm M}$ (for small values of $m_{\rm a}$).

The reason for the dominance of $W_{\rm L}$ over $Q_{\rm M}$ for small values of $m_{\rm a}$ is probably related to the relative dominant of the overall level of kinetic energy for small values of $m_{\rm a}$.

3.9.1 Possible sources of the late uprise of ρ_B

For progressively smaller axion mass, there is the development of a clear uprise in ρ_B at $N=9$–10. This time is well after the end of reheating, which is around $N=6$. It is also independent of numerical aspects, e.g. the value of $N_{\rm MHD}$, which we varied between $N_{\rm MHD}=1$ and 8, the value of $\mathrm{Pr_M}$, etc). However, since $B_{\rm rms}$ enters in the expression for σ_E, it can cause some feedback, especially when $m_{\rm a}$ is small. For small values of $m_{\rm a}$, $\mathcal{H}^{-1}$, and therefore also σ_E, increase, making this effect even more pronounced.

The strong uprise for small values of $m_{\rm a}$ is followed by an equally enhanced decay. This suggests that the increase in σ_E first leads to an increase in ρ_B, and then, as a consequence, to a longer value of $W_{\rm L}$.

Interestingly, the late-time bump in ρ_B does not lead to a pronounced feature in the diagnostic $B_{\rm rms}$ vs. $\xi_{\rm M}$ diagram. This is because of a correspondingly small decrease of $\xi_{\rm M}$ at the same time.

3.9.2 Possible sources of the hook after reheating

At the end of reheating, there is another pronounced feature in the magnetic field evolution. This time, it shows up quite clearly in the diagnostic $B_{\rm rms}$ vs. $\xi_{\rm M}$ diagram, and hardly at all in the individual evolutions of $B_{\rm rms}(N)$ and $\xi_{\rm M}(N)$. It corresponds to a small reduction in $\xi_{\rm M}(N)$, while the decay of $B_{\rm rms}(N)$ remains stagnant for that duration. This happens right after ρ_ϕ has decayed. One might therefore be tempted to associate this with the loss of the driving from the axion field. However, the axion field is already rather weak by that time, and also the associated growth rate is almost negligible, so this possibly seems unlikely. Another possibility is, again, related to the change in the conductivity. This is caused by the increase in the slope of $\mathcal{H}^{-1}$ from $\exp(N/2)$ to $\exp(N)$. To check this possibility, we have repeated the simulations using. ...

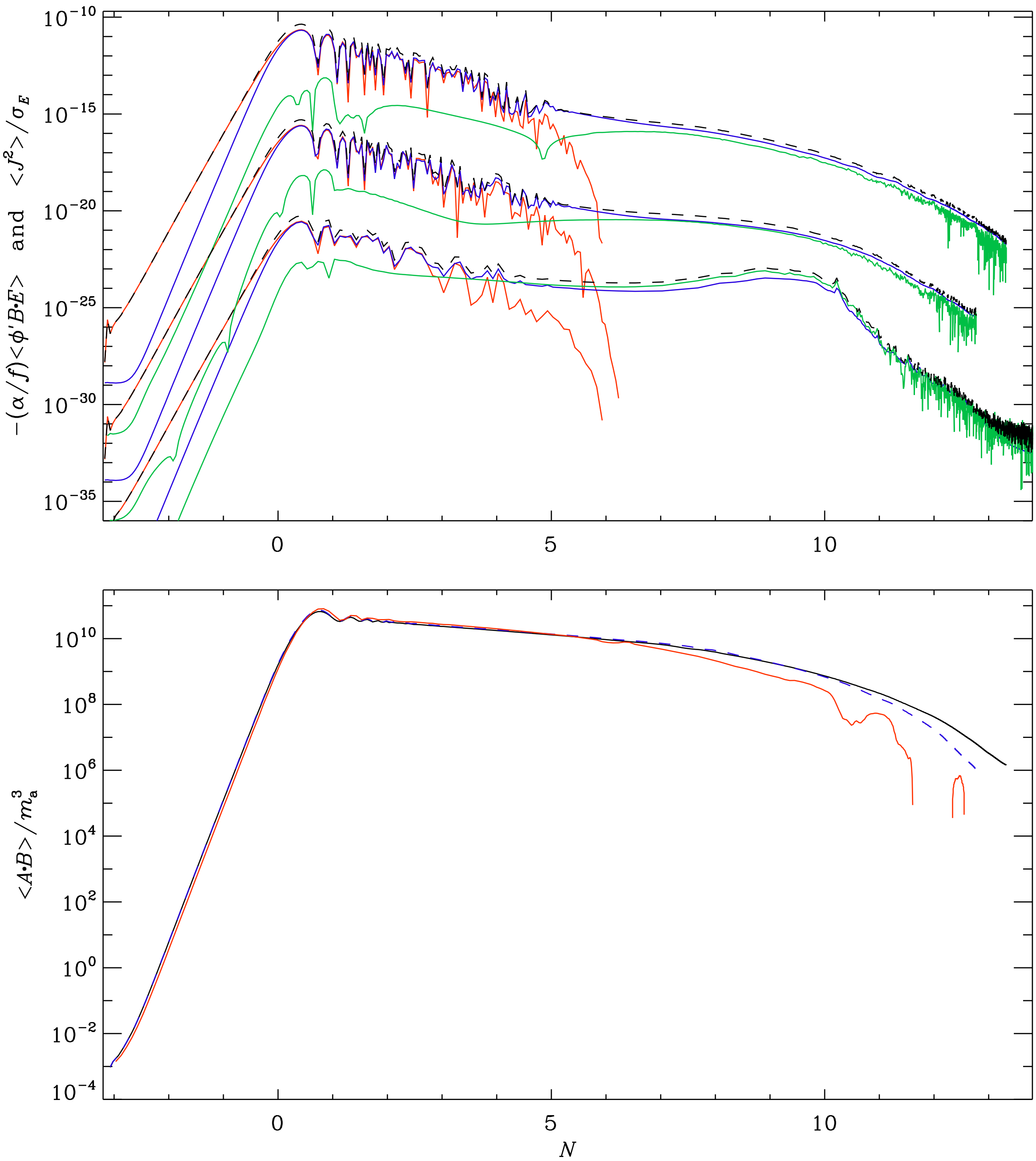

Figure 10. Time dependence of (a) $-\frac{\alpha}{f}\langle\phi'\boldsymbol{B}\cdot\boldsymbol{E}\rangle$ (red), $\langle\boldsymbol{J}^2/\sigma_E\rangle$, and $\langle\boldsymbol{u}\cdot(\boldsymbol{J}\times\boldsymbol{B})\rangle$, and (b) $\langle\mathbf{A}\cdot\boldsymbol{B}\rangle/m_{\rm a}^3$ for runs A, C, and E with 1024^3 mesh points. The o-run peaks at $N=9.5$, and if it is caused by the conductivity peak, why is this at $N=9.5$?

3.9.3 Dependent of the shape of the hook on the initial field strength

It runs out that the shape and extent of the hook in the diagnostic $B_{\rm rms}$ vs. $\xi_{\rm M}$ diagram depends on the value of the initial field strength. The hook represents a particular feature in this diagram as the system changes from reheating to radiation dominance. As explained above, it is associated with a sudden decrease in $\xi_{\rm M}$, while $B_{\rm rms}$ stays approximately stagnant.

The dependence of this feature on the initial field strength is shown in figure 12.

We see that, as we increase the initial field strength, the sudden drop in the length scale remains approximately unchanged, but the degree to which the field remains stagnant, becomes even more pronounced. Conversely, as we decrease the initial field strength, the value of $B_{\rm rms}$ is no longer really stagnant, but also drops. In this sense, the hook is a feature that is associated with a relative excess of magnetic energy. It also suggests that the system needs to dispose of as it enters the radiation dominant phase.

3.10 Dependence on the value of $\mathrm{Pr_M}$

The value of $\mathrm{Pr_M}$ parameterize our ignorance regarding the viscosity during Schwinger pair production. We recall that we are not concerned here with the viscosity that is applied already at the end of inflation and that is mainly needed for numerical reasons. As Schwinger pair production proceeds, the newly created particles will exert some viscosity on the motions, which has not been calculated yet.

In MHD, the viscosity has a similar effect on the velocity as the magnetic diffusivity, i.e., the inverse conductivity, has on the magnetic field. It smoothes out gradients in the velocity, just like the magnetic diffusivity smoothes out gradients in the magnetic field. Their ratio is the magnetic Prandtl number, $\mathrm{Pr_M} = \nu\sigma_E$. We considered here the values $\mathrm{Pr_M} = 1$, 10, and 100. The result is shown in figure 13.

In figure 13(a), we show how σ_E changes as we change the value of $\mathrm{Pr_M}$. We see that differences only emerge close to the end of reheating. Especially in the case when $\mathrm{Pr_M} = 1$, the system develops in a somewhat more vigorous way and leads to slightly larger velocities and thereby also to stronger magnetic fields.

This also has consequences for the conductivity itself, because it is proportional to the magnetic field strength. This generally requires larger numerical resolution. At fixed resolution, however, as shown in figure 13, the simulations for $\mathrm{Pr_M} = 1$ eventually diverges.

Conversely, at large values, for $\mathrm{Pr_M} = 100$, the system develops less vigorously and reaches smaller velocities and smaller magnetic fields. Therefore, also the conductivity itself does not grow as much.

Comparing the time evolutions of the various energy densities for different values of $\mathrm{Pr_M}$, we see that the most pronounced change occurs when the magnetic field drops at around $N = 9$. For $\mathrm{Pr_M} = 1$, this drop is relatively strong in the magnetic field, and almost entirely absent in the mean kinetic energy density.

3.11 Built-up of magnetic helicity

An important feature of action inflation is a generation of a helical magnetic field, i.e., $\langle \boldsymbol{A} \cdot \boldsymbol{B}\rangle \neq 0$. This is significant once the conductivity is sufficiently large, because only then $\langle \boldsymbol{A} \cdot \boldsymbol{B}\rangle$ is approximately conserved when $\langle \rho_\phi \rangle$ has become negligible.

For the purpose of extracting the magnetic helicity equation, we dot equation (2.22) with $\boldsymbol{B}$ and obtain

$$\frac{d}{d\tau}\langle \boldsymbol{A} \cdot \boldsymbol{B}\rangle = 2\sigma_E^{-1}\left(\langle \Lambda_0 \boldsymbol{B}^2\rangle - \langle \boldsymbol{B} \cdot \boldsymbol{\nabla} \times \boldsymbol{B}\rangle\right) + G_{Faraday} + G_{rest} \tag{3.2}$$

where $G_{Faraday} = 2\langle \boldsymbol{B} \cdot \partial \boldsymbol{E}/\partial\tau\rangle$ is a term resulting from the Faraday displacement current, and $G_{rest} = \langle \boldsymbol{B} \cdot \boldsymbol{\Delta}(\Lambda_0 \boldsymbol{B}^2\rangle - \langle \boldsymbol{B} \cdot \boldsymbol{\nabla} \times \boldsymbol{B}\rangle)$ is a rest term. Both dissipation and generation terms are proportional to σ_E^{-1}, so they are only important for intermediate values of the conductivity before it becomes high too high.

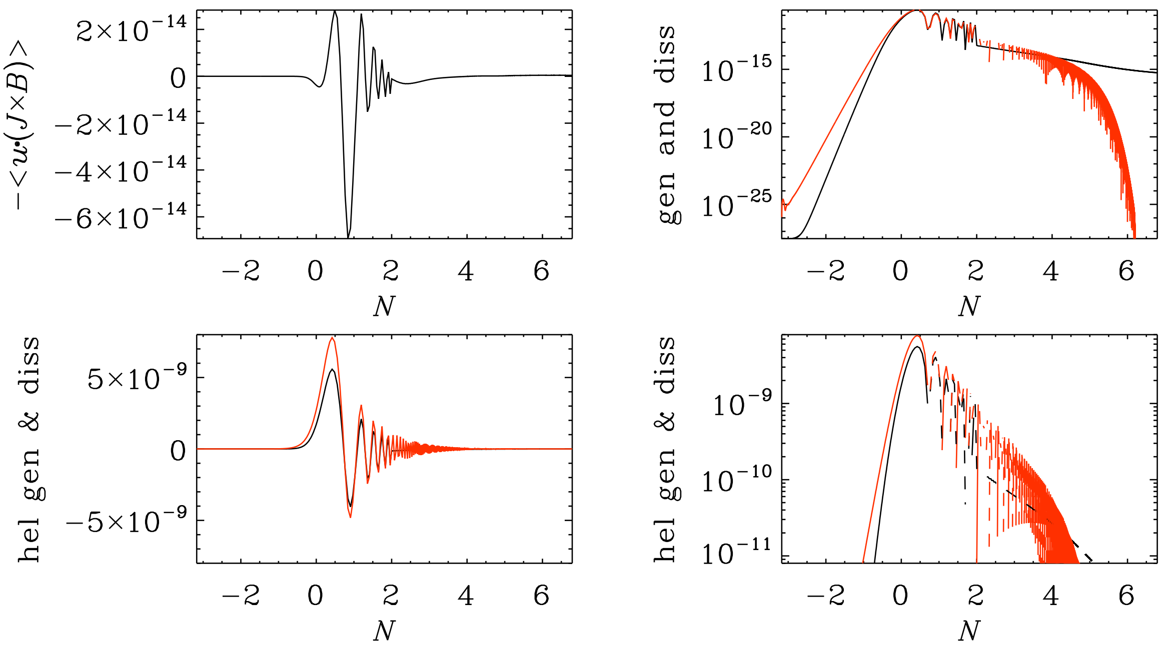

Figure 11. Time dependence of work done against the Lorentz force (left) and magnetic energy generation and dissipation (right) in red and black. [**AB**: Need a spectral version of the work term.]

[**AB**: The rest should go elsewhere, if at all!] For the evolution of the electromagnetic energy, we have

$$\frac{1}{2}\frac{d}{d\tau}\langle \boldsymbol{E}^2+\boldsymbol{B}^2\rangle = \left(-\frac{\alpha}{f}\langle\phi'\boldsymbol{B}\cdot\boldsymbol{E}\rangle - \langle\boldsymbol{J}\cdot\boldsymbol{E}\rangle\right), \tag{3.3}$$

The result is shown in figure 11 for Run A. It is particularly revealing to investigate the scale dependence of the rhs by inspecting the shell-integrated spectrum

$$-\frac{\alpha}{f}\left(\widetilde{\phi'\boldsymbol{B}}\right)_k\cdot\left(\widetilde{\boldsymbol{E}}\right)_k^*. \tag{3.4}$$

3.12 Spectra near the hook in the evolutionary track

The hook in the evolutionary track is related to the dissipation of the inflaton. However, other than through the $\boldsymbol{E}\cdot\boldsymbol{B}$ backreaction term in equation (2.1), there is no direct connection between inflaton and the magnetic field (this will be demonstrated later). To illuminate this puzzle, we plot in figure **??** and figure 17 the spectra of electric and magnetic field, the bulk velocity, the density variance, and $E_\phi(k,\tau)$ along with the diagnostic diagram where the times of the spectra are indicated.

3.13 Inverse cascade during and after reheating

Both during and after reheating, we see clear signs of an inverse cascade. At the same time, there is always also a forward cascade. The types of cascade behaviors can be presented in four different phases. In the first phase, we see the build-up of magnetic energy at low wave numbers; see figure 16. This phase is then ...

Loss of magnetic helicity.

Growth of σ_E.

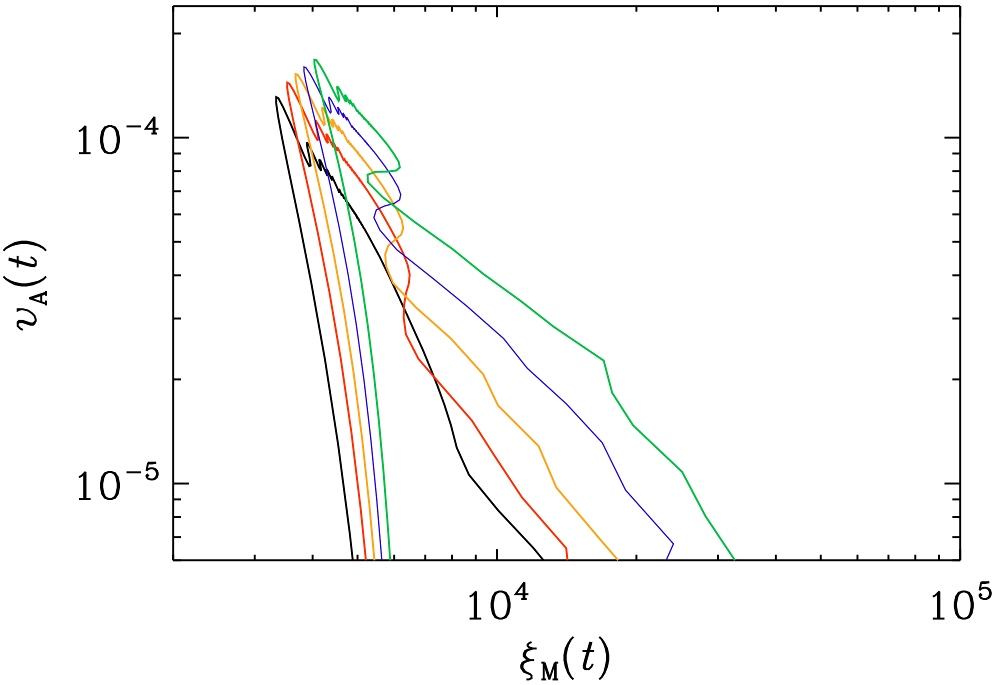

Figure 12. Dependence of the strength of the hook on the initial field strength (varying by factors 0.2, 0.5, 1, 2, and 5) for different versions of Run A.

3.14 Evolution of conductivity

It turns out that in all runs, the value of σ_E first decreases with time. This is mostly because of the initial increase of $\mathcal{H}$ while $B_{\rm rms}$ and $E_{\rm rms}$ stay approximately constant. After that, σ_E increases approximately quadratically with a. This is because of a similar increase of $B_{\rm rms}$. At some time ($\tau m_{\rm a} \approx 0.16$), τ_σ reaches an initial peak, continues to oscillate for some time, and then shows a continued increase owing to the increase of $\mathcal{H}^{-1} \propto a$.

```
Run  ma   erms Gamph0 numax  run
A  1e-5  1e-10  1e-8  2e4  Hbdm512alpf90_sig1_rho24_ampl1_Gam8b' & m1=1e-5  ;(good, follows
B  1e-5  1e-10  1e-9  2e4  Hbdm512alpf90_sig1_rho24_ampl1_Gam9b' & m2=1e-5  ;(good, agrees
C  1e-6  1e-12  1e-9  2e4  Hbdn512alpf90_sig01_rho28_ampl1_Gam9c' & m3=1e-6 ;(longer reheat
D  1e-6  1e-12  1e-10 2e4  Hbdn512alpf90_sig01_rho28_ampl1_Gam10b' & m4=1e-6 ;(longer rehea
E  1e-7  1e-14  1e-11 2e4  Hbdo512alpf90_sig001_rho32_ampl1_Gam11c
```

In figure 18, we show that the inflaton spectrum is very small when the $\boldsymbol{E}\cdot\boldsymbol{B}$ backreaction term in equation (2.1) is omitted, which is called the linear regime. This shows that when this term is included, the inflaton spectrum is driven by the electromagnetic fields and cannot itself drive or explain the evolution of the magnetic field. It is therefore also not directly responsible for causing the hook.

The main change in the spectra both in the linear and the full....

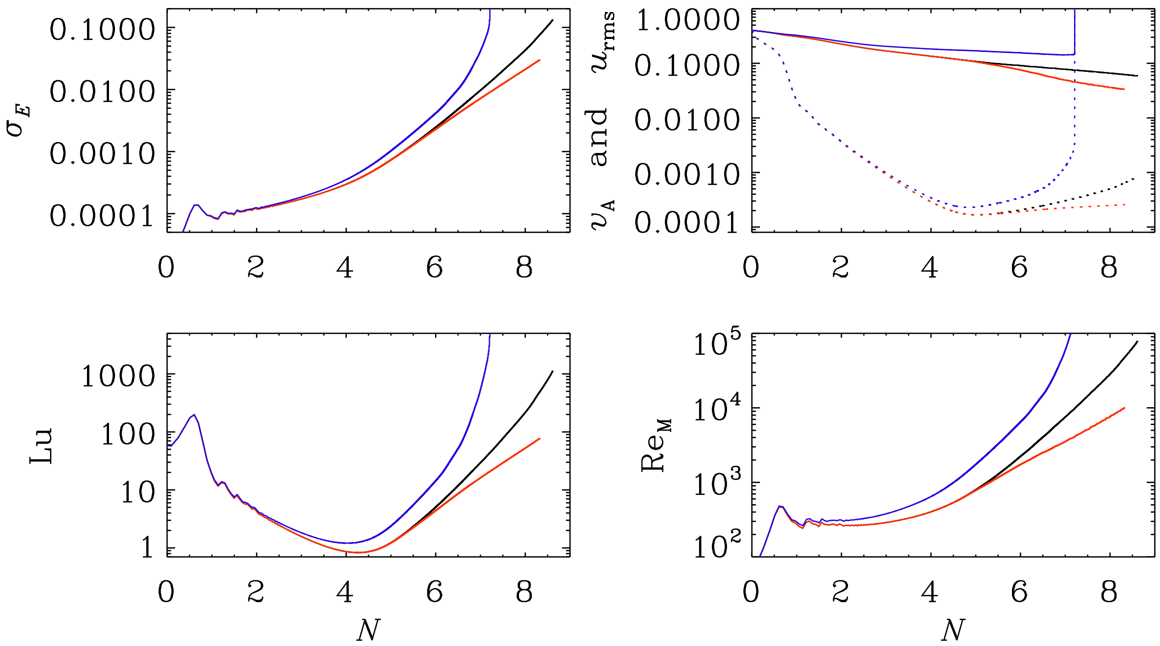

Figure 13. Evolution of σ_E, $v_{\rm A}$ (solid lines) and $u_{\rm rms}$ (dotted lines), Lu, and $\mathrm{Re_M}$ for runs with $m_{\rm a} = 10^{-7}$ and $\mathrm{Pr_M} = 1$ (blue), 10 (black), and 100 (red).

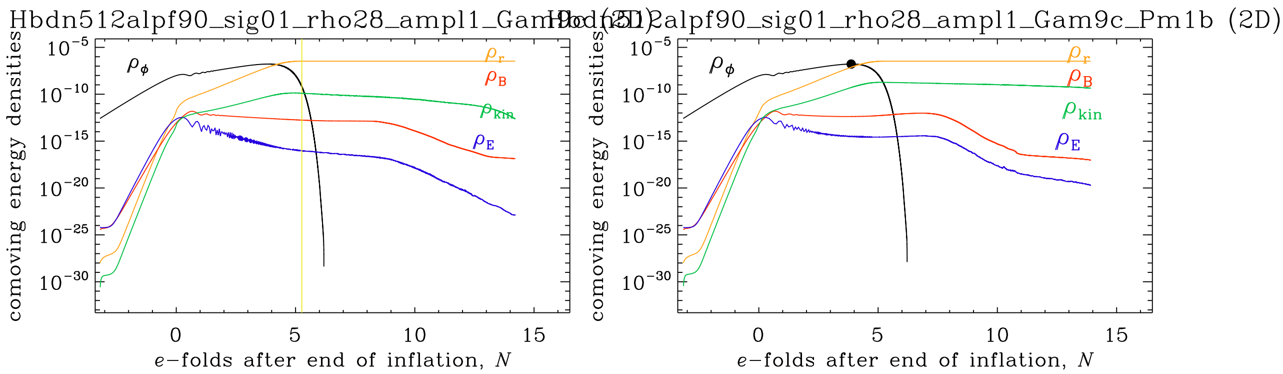

Figure 14. Comparison between $\mathrm{Pr_M} = 10$ (left) and $\mathrm{Pr_M} = 1$ (right). **[AB**: To add also $\mathrm{Pr_M} = 1$.]

3.15 Comparison with the conductivity of quark–gluon plasmas

The conductivity prescription of equation (2.8) was derived for a Schwinger pair plasma, which is relevant to the era of reheating. It underestimates the number of species compared to a quark–gluon plasma. At later times, when a quark–gluon plasmas has been fully established, the prescription of equation (2.8) can no longer be relevant. Here we compare with the conductivity prescription of ref. [35] that was derived for very hot plasmas.

According to eq. (1.10) of ref. [35], the conductivity of a quark–gluon plasma is given by $\sigma_E = CT/(e^2 \ln e^{-1})$, where $C \approx 12$ is a dimensionless coefficient and $e = 0.303$. We estimate the temperature T from equation (2.10) by assuming that all the energy is given by

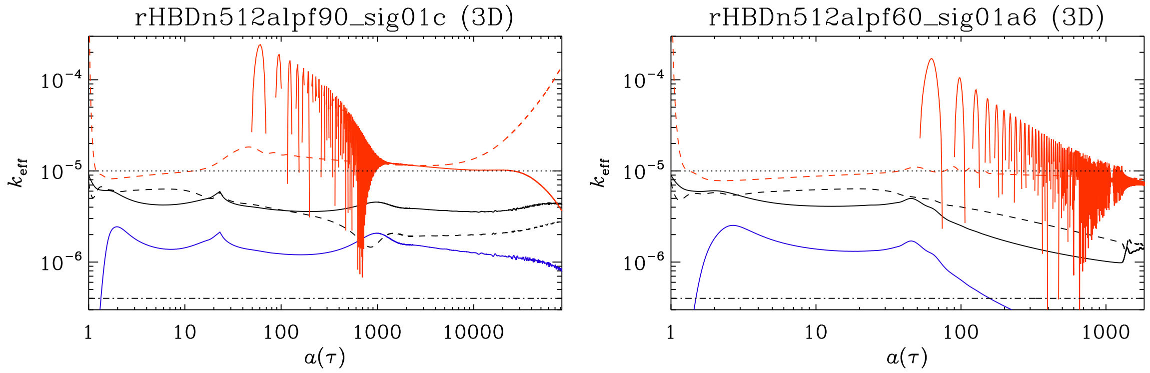

Figure 15. Characteristic wave numbers: k_ω (solid black), $k_{\nabla\cdot\boldsymbol{u}}$ (dashed black), $k_{\boldsymbol{\omega}\cdot\boldsymbol{u}}$ (blue), $k_{\boldsymbol{J}\cdot\boldsymbol{B}}$ (solid red), $k_{\boldsymbol{A}\cdot\boldsymbol{B}}$ (dashed red). The dashed-dotted horizontal line denotes the value of k_1. the dotted horizontal line denotes the value of $k_{\rm p}$.

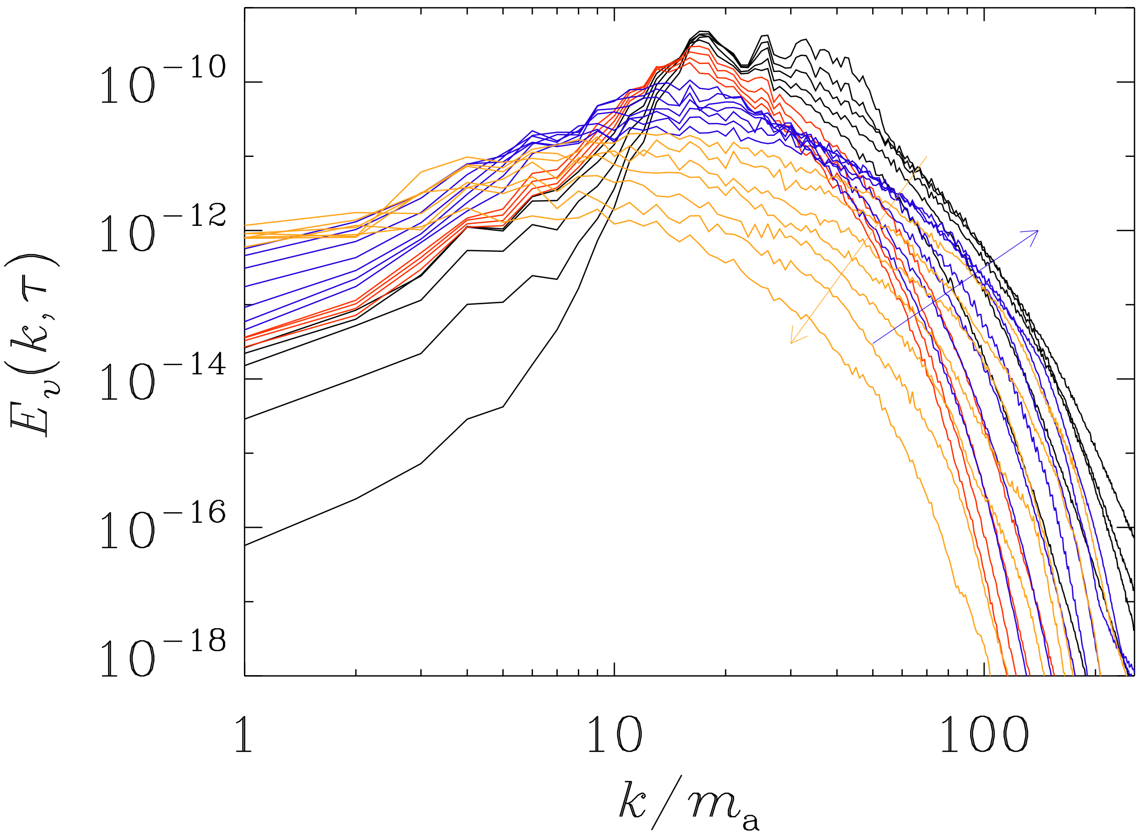

Figure 16. Magnetic spectra in 4 groups.

$(\pi^2/30)\, g_{\rm e} T^4$ using $g_{\rm e} = 106.75$.

The result is shown in figure 19 our models with $m_{\rm a} = 10^{-5}$, 10^{-6}, and 10^{-7}. We see that the value from eq. (1.10) of ref. [35] yields generally larger values after reheating, but

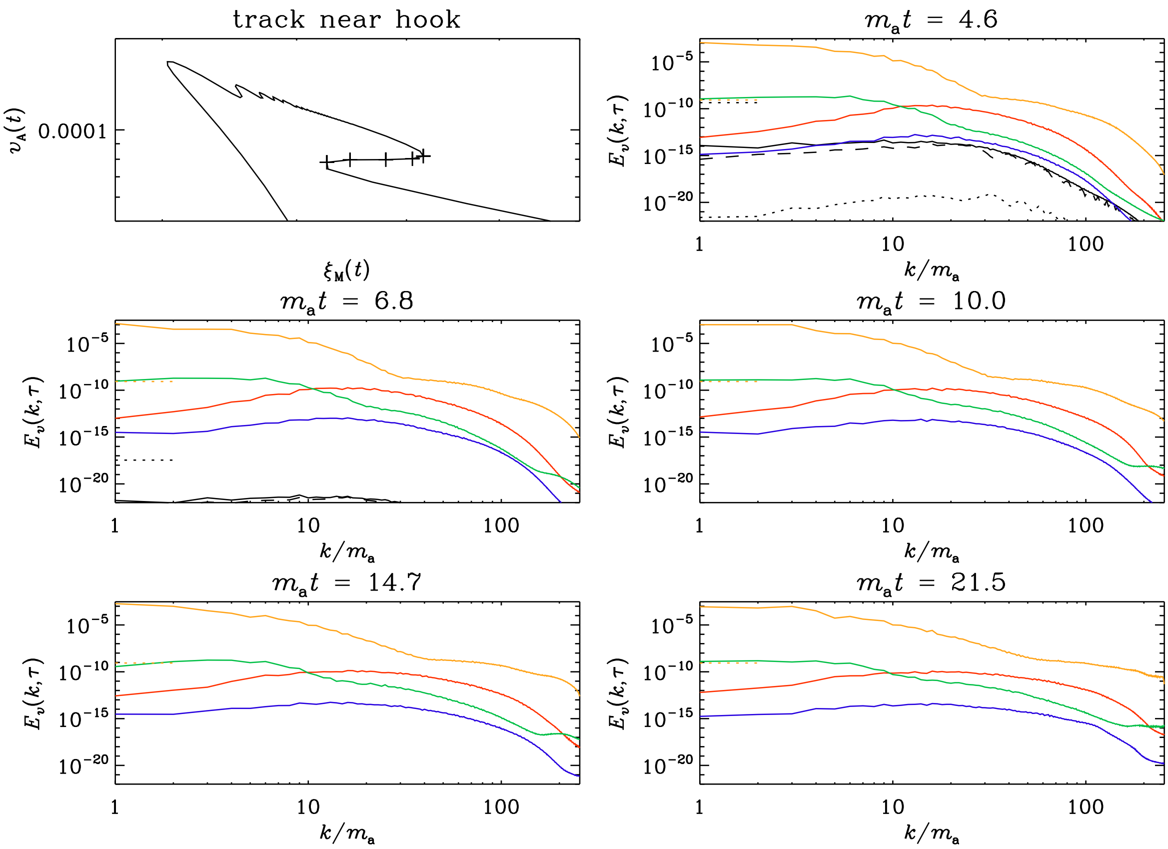

Figure 17. Close-up of the evolutionary track near the hook together with spectra of electric (blue) and magnetic field (red), bulk velocity (green), density variance (orange), and $E_\phi(k,\tau)$ (black solid), as well as the contributions from $(a^2/2)\mathrm{Sp}(\phi')$ (dotted black) and $(a^2/2)\mathrm{Sp}(\boldsymbol{\nabla}\phi)$ (dashed black). The dominant contribution to $E_\phi(k,\tau)$ always comes from $(a^4/2)m_\mathrm{a}\mathrm{Sp}(\phi)$.

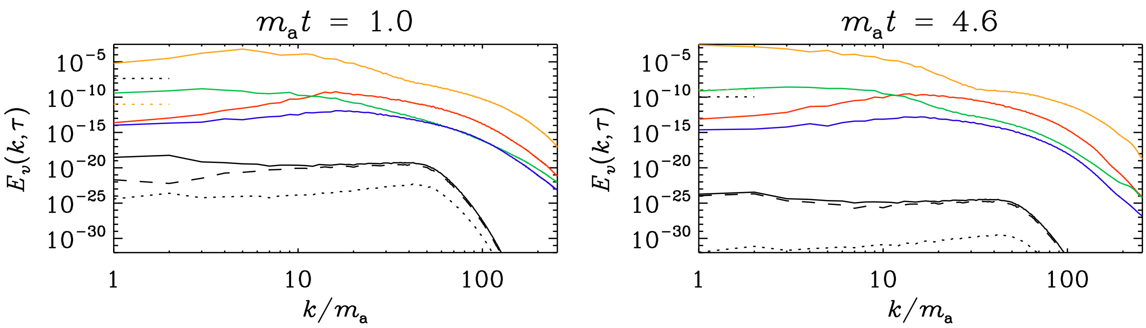

Figure 18. Spectra similar to figure 17, but for a run without the $\boldsymbol{E}\cdot\boldsymbol{B}$ backreaction term in equation (2.1). Note that the scale on the vertical axis has been extended to capture the comparatively weak $E_\phi(k,\tau)$ spectrum.

since they are decreasing with time, while those from equation (2.8) are increasing, the two would cross at some point. This is the case at $N \approx 8$–10, depending on the value of m_a. In

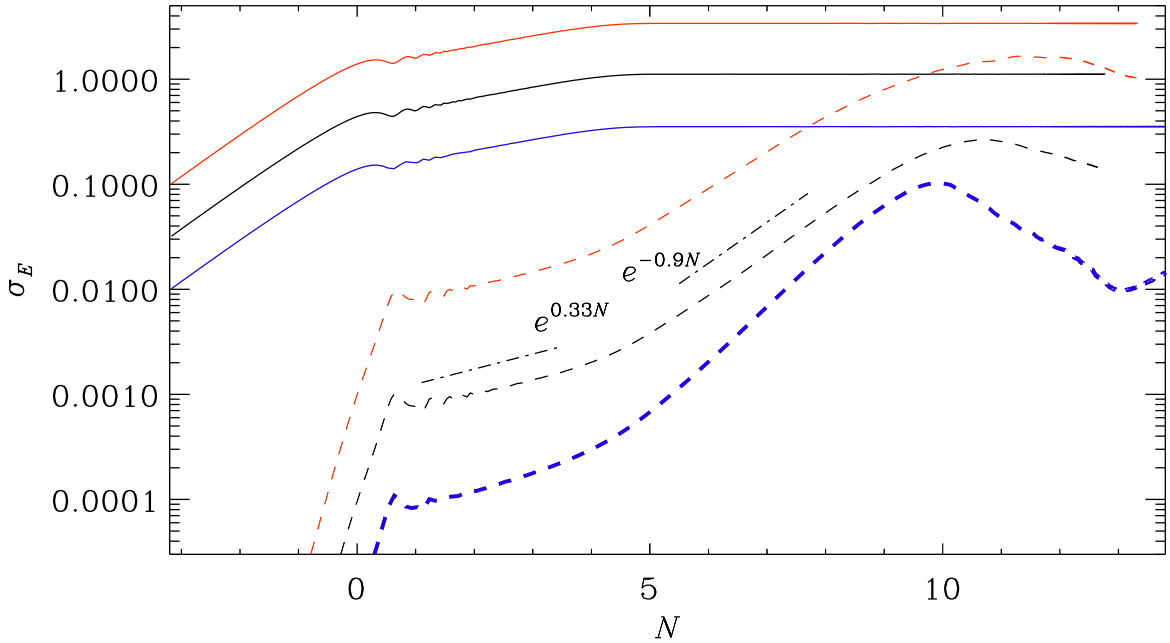

Figure 19. Dependence of the comoving values of σ_E from our model using equation (2.8) (dashed lines) with eq. (1.10) of ref. [35] (solid lines) for $m_a = 10^{-5}$ (red lines), 10^{-6} (black lines), and 10^{-7} (blue lines). Note that the value from eq. (1.10) of ref. [35] yields generally larger values after reheating, but since they are decreasing with time, while those from equation (2.8) are increasing, the two would cross at some point.

conclusion, one can say that, although the two formulae for σ_E are very different from each other, the resulting values are still surprisingly similar.

It also turns out that the case with $m_a = 10^{-7}$ is different in that σ_E starts to increase more sharply after the end of reheating than for the other two runs. This is a consequence of the slight increase of the magnetic field in connection with the rather pronounced bump for small values of m_a.

3.16 Lundquist and magnetic Reynolds numbers

The MHD evolution becomes highly nonlinear due to the growing dominance of the nonlinear terms $\boldsymbol{u} \times \boldsymbol{B}$ in the induction equation and $\boldsymbol{u} \cdot \boldsymbol{\nabla} \boldsymbol{u}$ in the momentum equation. Their competition with the linear resistive and viscous terms is quantified by the Lundquist and Reynolds numbers, respectively. Except for the early times, the Reynolds number and the magnetic Reynolds number are related to each other through the prescribed magnetic Prandtl number $\mathrm{Pr_M}$, i.e., $\mathrm{Re_M} = \mathrm{Pr_M}\mathrm{Re}$. In figure 20, we have plotted Lu and $\mathrm{Re_M}$. We see that the value of Lu is generally below 100, while $\mathrm{Re_M}$ can reach much larger values between 10^3 and 10^4.

In table 2, we summarize for these 3 runs the values of Lu and $\mathrm{Re_M}$. For all three runs, both values go through a minimum at $N \approx 4$, so we give the values of Lu and $\mathrm{Re_M}$ both at $N = 4$ and at $N = 8$, which is when the conductivity from eq. (1.10) of ref. [35] begins to apply. We see that for $m_a = 10^{-7}$, the values of Lu drop to rather low values below unity so that magnetic helicity conservation becomes a poor assumption. Even for $m_a = 10^{-6}$, Lu has

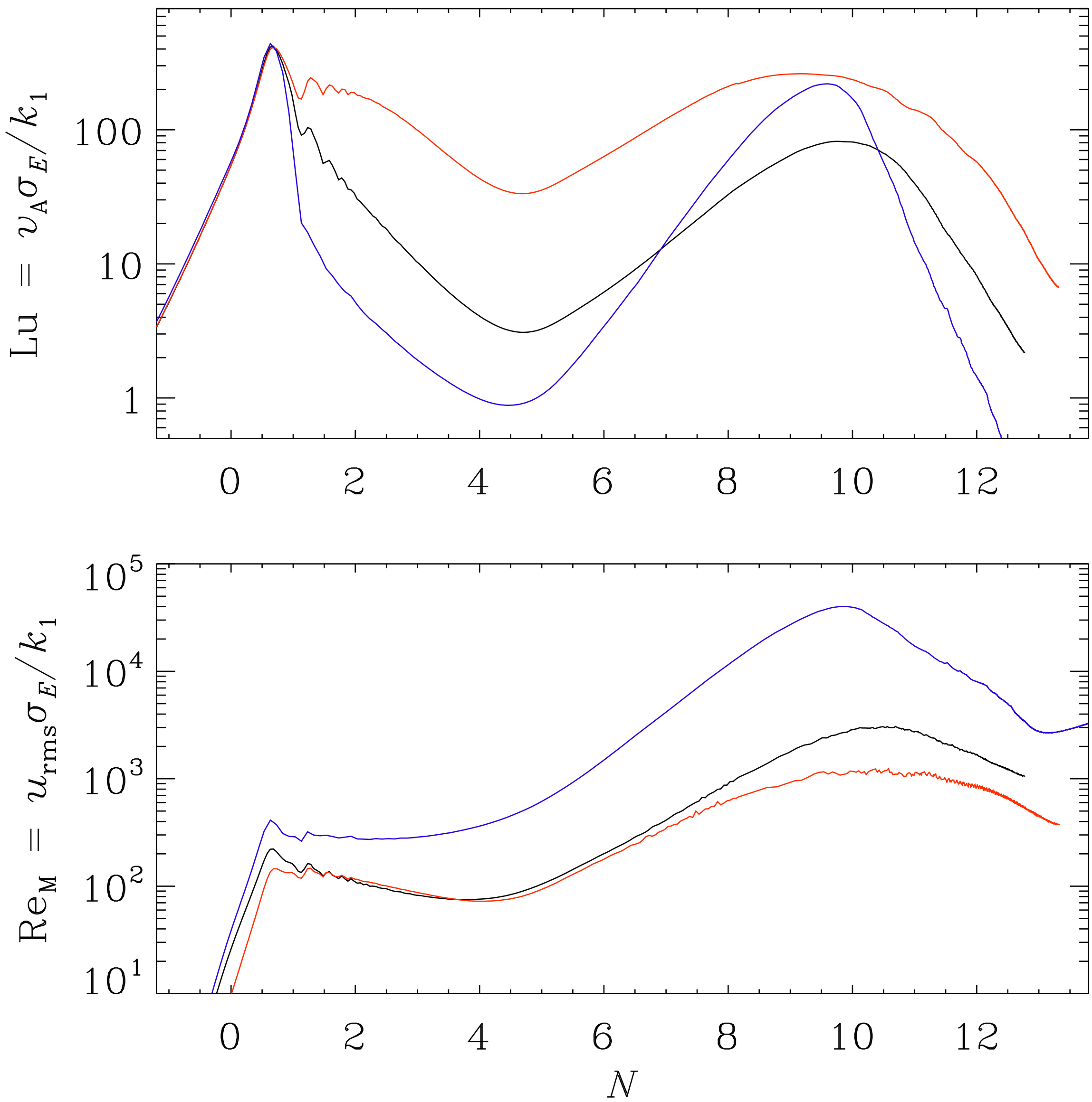

Figure 20. Dependence of Lundquist and magnetic Reynolds numbers for $m_\mathrm{a} = 10^{-5}$ (red lines), 10^{-6} (black lines), and 10^{-7} (blue lines).

Table 2. Summary of Lundquist numbers as well as kinetic and magnetic Reynolds numbers. The parentheses indicate uncertainty.

Run	m_a	Γ_ϕ	$\mathrm{Lu}(N = 4 \rightarrow 8)$	$\mathrm{Re_M}(N = 4 \rightarrow 8)$
A	10^{-5}	10^{-8}	$60 \rightarrow 700$	$100 \rightarrow 1000$
C	10^{-6}	10^{-9}	$5 \rightarrow 120$	$100 \rightarrow 1800$
E	10^{-7}	10^{-10}	$0.8 \rightarrow 360$	$400(\rightarrow 26000)$

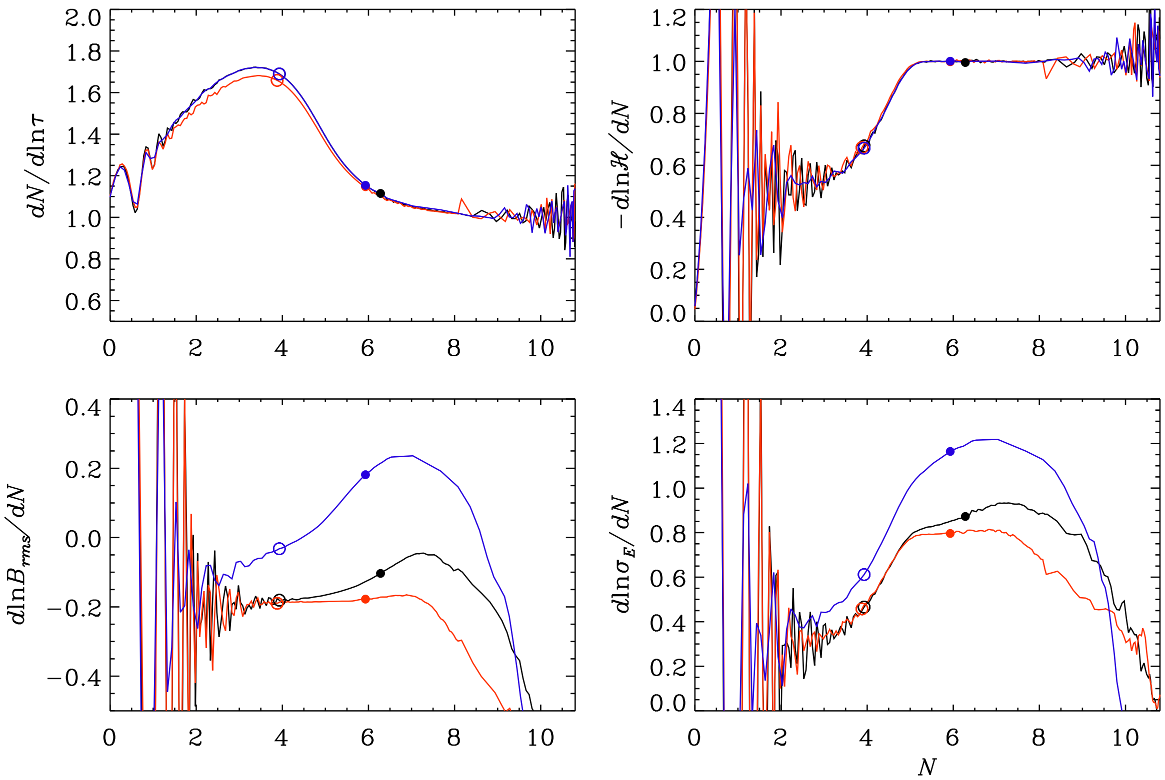

Figure 21. Dependence of the instantaneous scaling exponents on N for $m_{\rm a} = 10^{-5}$ (red lines), 10^{-6} (black lines), and 10^{-7} (blue lines).

a minimal value of around 5. On for $m_{\rm a} = 10^{-5}$, we have $\mathrm{Lu} \approx 60$, which is large enough so that magnetic helicity becomes reasonably well conserved.

Generally, Lu is the largest when $m_{\rm a}$ is the largest. This is because in Lu, the product of $v_{\rm A}$ and σ_E enters, and when $v_{\rm A}$ is large, also σ_E is large as a consequence. The situation is different for $\mathrm{Re}_{\rm M}$. Although here too, σ_E enters in the numerator, the value of $\mathrm{Re}_{\rm M}$ is the largest for the smallest value of $m_{\rm a}$. This is caused by the large rms velocity, which retains larger values as $m_{\rm a}$ decreases. This is primarily a consequence of the quadratic scaling of $\rho_{\rm kin}$ with $m_{\rm a}$, as opposed to the quartic scaling of ρ_B.

3.17 Origin of the late uprise of magnetic energy

The late uprise of the magnetic energy is likely caused by the rise in the conductivity, which allows the plasma motions to amplify the magnetic field by stretching it. To understand the origin of the late increase in the conductivity, we recall that $\sigma_E \approx 0.004 \times |\boldsymbol{B}|/\mathcal{H}$. The local double-logarithmic slopes of $B_{\rm rms}$ and $1/\mathcal{H}$ are plotted in figure 21. At the beginning of the radiation-dominated era ($N \approx 6$), we have $1/\mathcal{H} \sim e^N$. For Runs A, C, and E, we have $B_{\rm rms} \sim e^{-0.18}$, $\sim e^{-0.2}$, and $\sim e^{+0.2}$, respectively. This corresponds to $\sigma_E \sim e^{0.8}$, $\sim e^{0.9}$, and $\sim e^{1.2}$, which is in good agreement with what is seen in figure 19.

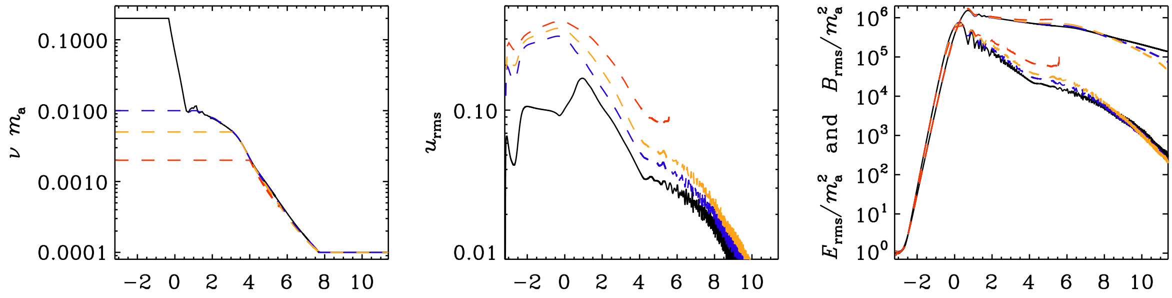

Figure 22. Time dependence of $u_{\rm rms}$, $E_{\rm rms}$, and $B_{\rm rms}$ on the initial and early-time viscosity for Run A with $\nu_{\rm max} = 2 \times 10^4$ (black), $\nu_{\rm max} = 10^3$ (blue), $\nu_{\rm max} = 5 \times 10^2$ (orange), and $\nu_{\rm max} = 2 \times 10^2$ (red).

3.18 Dependence on the early value of the viscosity

As we have stated in the beginning, a certain viscosity is needed even in the beginning of the simulation, when no plasma exists yet. However, it is not quite true that no plasma exists yet, because even a very small value of the magnetic field produces a finite conductivity; see equation (2.15) and the approximations $\sigma_E \approx 0.004 \times |\boldsymbol{B}|/\mathcal{H}$.

Therefore, the Lorentz force is nonvanishing and, especially for very small initial values of the radiation energy density, the resulting acceleration per unit mass is large. To keep the flow stable for a fixed resolution, some small viscosity is needed.

In figure 22, we show the time dependence of ν normalized by $m_{\rm a}$, as well as $u_{\rm rms}$ together with $E_{\rm rms}$ and $B_{\rm rms}$. We see that the effect on $E_{\rm rms}$ and $B_{\rm rms}$ is small, but the values of $u_{\rm rms}$ change more strongly in that small values of ν result in larger velocities.

4 Saturation of the magnetic field

To investigate the mechanisms leading to magnetic field saturation, we can manipulate various terms in the equations. We can study the response to σ_E by reducing or enhancing the prefactor in front of the expression for σ_E.

4.1 Vorticity and kinetic helicity

Unlike kinetic energy production from potential energy, where the forcing is proportional to the gradient of the gravitational potential (and therefore curl-free), the velocity from magnetogenesis is likely to produce significant amounts of helicity.

Here, we quantify the amount of mean-squared vorticity production, $\langle\boldsymbol{\omega}^2\rangle$, where $\boldsymbol{\omega} = \boldsymbol{\nabla} \times \boldsymbol{u}$ is the vorticity; see figure 15. We also expect the kinetic helicity density, $\langle\boldsymbol{\omega} \cdot \boldsymbol{u}\rangle$, to be different from zero

5 Conclusions

Our work has demonstrated an unexpected dominance of velocity fluctuations over the generated magnetic field fluctuations. This leads to faster decay laws of the magnetic field than what was previously expected when the velocity field is small. The prospects of explaining primordial magnetic fields from axion inflation remain difficult—at least for the parameters

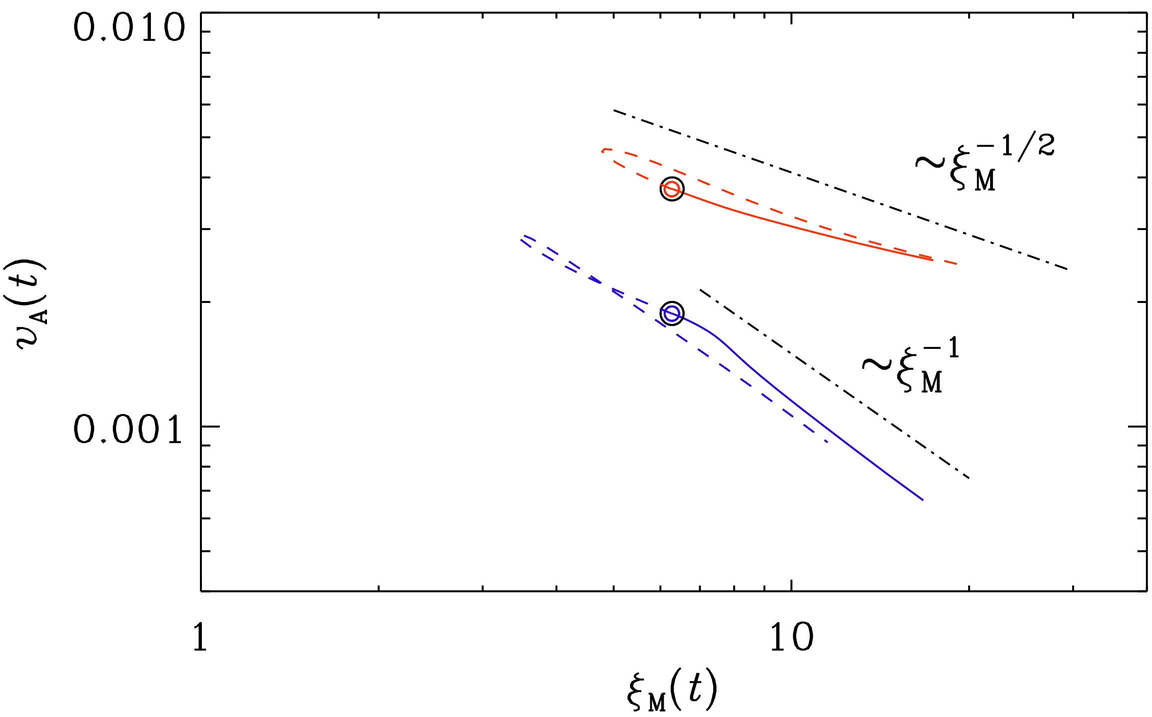

Figure 23. Decay for a 2D helical field without initial velocity field (red solid line) and with initial velocity (red dashed line), and for a 2D nonhelical field without initial velocity field (blue solid line) and with initial velocity (blue dashed line).

studied in this work, which confirms our earlier findings for axion inflation with Schwinger pair production.

The conductivity of between 0.3 to 3 for o- and m-runs is not so large, but the magnetic field is simply not larger enough to make the Lundquist number large enough. Note also that the time derivative of $B_{\rm rms}$ peaks earlier than $B_{\rm rms}$ itself.

Originally we had expected that σ_E is always much larger than what is possible to simulate numerically. While this may still well be true, it is not the case in our present models. This might well be a consequence of the relatively weak magnetic fields that have been obtained in our models.

A 1D, 2D, and 3D axion inflation with radiation

B Effect of initial velocity on 2D decay with helicity

In figure 23, we show the decay for 2D helical and nonhelical fields with and without initial velocity fields. Regardless of the initial velocity field, the decay approaches the expected $v_A \propto \xi_M^{-1/2}$ law in the helical case, and the $v_A \propto \xi_M^{-1}$ law in the strictly 2D nonhelical case.

References

[1] W.D. Garretson, G.B. Field and S.M. Carroll, *Primordial magnetic fields from pseudo Goldstone bosons*, *Phys. Rev. D* **46** (1992) 5346 [hep-ph/9209238].

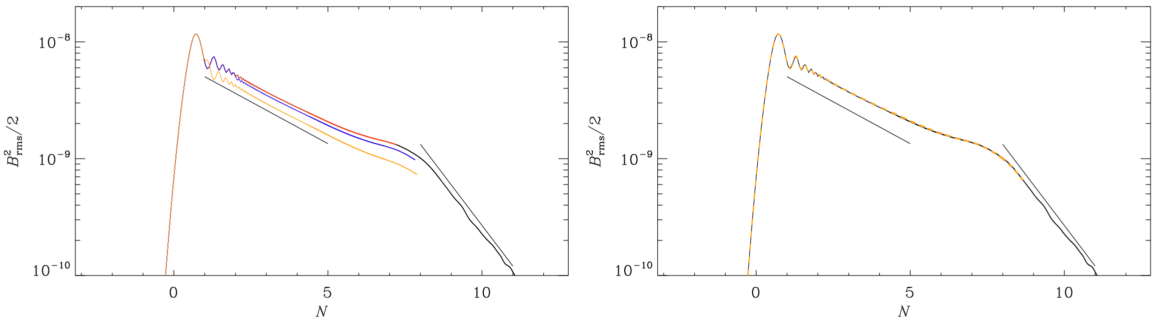

Figure 24. Left: old results for magnetic decay for m-runs with different MHD switches: $N_{\rm MHD} = 1$, 2, 4, and 7. Right: corrected result for $N_{\rm MHD} = 1$, compared with $N_{\rm MHD} = 7$. Both for m-runs `Hbdm512alpf90_rho24_ampl1_Gam8o_aBE_ee1_cor`.

[2] M.M. Anber and L. Sorbo, *N-flationary magnetic fields*, *JCAP* **10** (2006) 018 [astro-ph/0606534].

[3] T. Fujita, R. Namba, Y. Tada, N. Takeda and H. Tashiro, *Consistent generation of magnetic fields in axion inflation models*, *JCAP* **05** (2015) 054 [1503.05802].

[4] P. Adshead, J.T. Giblin, T.R. Scully and E.I. Sfakianakis, *Magnetogenesis from axion inflation*, *JCAP* **10** (2016) 039 [1606.08474].

[5] R. Durrer, O. Sobol and S. Vilchinskii, *Backreaction from gauge fields produced during inflation*, *Phys. Rev. D* **108** (2023) 043540 [2303.04583].

[6] F. Sauter, *Uber das Verhalten eines Elektrons im homogenen elektrischen Feld nach der relativistischen Theorie Diracs*, *Z. Phys.* **69** (1931) 742.

[7] W. Heisenberg and H. Euler, *Consequences of Dirac's theory of positrons*, *Z. Phys.* **98** (1936) 714 [physics/0605038].

[8] J.S. Schwinger, *On gauge invariance and vacuum polarization*, *Phys. Rev.* **82** (1951) 664.

[9] Y. Kluger, J.M. Eisenberg, B. Svetitsky, F. Cooper and E. Mottola, *Fermion pair production in a strong electric field*, *Phys. Rev. D* **45** (1992) 4659.

[10] A. Brandenburg, K. Enqvist and P. Olesen, *Large-scale magnetic fields from hydromagnetic turbulence in the very early universe*, *Phys. Rev. D* **54** (1996) 1291 [astro-ph/9602031].

[11] M. Christensson, M. Hindmarsh and A. Brandenburg, *Inverse cascade in decaying 3-D magnetohydrodynamic turbulence*, *Phys. Rev. E* **64** (2001) 056405 [astro-ph/0011321].

[12] R. Banerjee and K. Jedamzik, *The Evolution of cosmic magnetic fields: From the very early universe, to recombination, to the present*, *Phys. Rev. D* **70** (2004) 123003 [astro-ph/0410032].

[13] J. Reppin and R. Banerjee, *Nonhelical turbulence and the inverse transfer of energy: A parameter study*, *Phys. Rev. E* **96** (2017) 053105 [1708.07717].

[14] P. Trivedi, J. Reppin, J. Chluba and R. Banerjee, *Magnetic heating across the cosmological recombination era: results from 3D MHD simulations*, *Mon. Not. R. Astron. Soc.* **481** (2018) 3401 [1805.05315].

[15] A. Brandenburg, Y. He, T. Kahniashvili, M. Rheinhardt and J. Schober, *Relic Gravitational Waves from the Chiral Magnetic Effect*, *Astrophys. J.* **911** (2021) 110 [2101.08178].

[16] A. Brandenburg and R. Sharma, *Simulating Relic Gravitational Waves from Inflationary Magnetogenesis*, *Astrophys. J.* **920** (2021) 26 [2106.03857].

[17] A. Brandenburg, Y. He and R. Sharma, *Simulations of Helical Inflationary Magnetogenesis and Gravitational Waves*, *Astrophys. J.* **922** (2021) 192 [2107.12333].

[18] A. Brandenburg and N.N. Protiti, *Electromagnetic Conversion into Kinetic and Thermal Energies*, *Entropy* **25** (2023) 1270 [2308.00662].

[19] O. Iarygina, E.I. Sfakianakis and A. Brandenburg, *Schwinger effect in axion inflation on a lattice*, 2506.20538.

[20] P. Adshead, J.T. Giblin, M. Pieroni and Z.J. Weiner, *Constraining axion inflation with gravitational waves from preheating*, *Phys. Rev. D* **101** (2020) 8 [1909.12842].

[21] L.D. Landau and E.M. Lifshitz, *Fluid Mechanics* (1987).

[22] E. Carretti and F. Vazza, *Radio Observations as a Probe of Cosmic Web Magnetism*, *Universe* **11** (2025) 164 [2505.18619].

[23] MAGIC collaboration, *A lower bound on intergalactic magnetic fields from time variability of 1ES 0229+200 from MAGIC and Fermi/LAT observations*, *Astron. Astrophys.* **670** (2023) A145 [2210.03321].

[24] Particle Data Group collaboration, *Review of Particle Physics*, *Chin. Phys. C* **38** (2014) 090001.

[25] P. Adshead, J.T. Giblin, T.R. Scully and E.I. Sfakianakis, *Gauge-preheating and the end of axion inflation*, *JCAP* **12** (2015) 034 [1502.06506].

[26] A. Roper Pol and A. Salvino Midiri, *Relativistic magnetohydrodynamics in the early Universe*, *arXiv e-prints* (2025) arXiv:2501.05732 [2501.05732].

[27] R. von Eckardstein, K. Schmitz and O. Sobol, *On the Schwinger effect during axion inflation*, *Journal of High Energy Physics* **2025** (2025) 96 [2408.16538].

[28] E. Bavarsad, S.P. Kim, C. Stahl and S.-S. Xue, *Effect of a magnetic field on Schwinger mechanism in de Sitter spacetime*, *Phys. Rev. D* **97** (2018) 025017 [1707.03975].

[29] V. Domcke and K. Mukaida, *Gauge Field and Fermion Production during Axion Inflation*, *JCAP* **11** (2018) 020 [1806.08769].

[30] V. Domcke, Y. Ema and K. Mukaida, *Chiral Anomaly, Schwinger Effect, Euler-Heisenberg Lagrangian, and application to axion inflation*, *JHEP* **02** (2020) 055 [1910.01205].

[31] S. Candelaresi, A. Hubbard, A. Brandenburg and D. Mitra, *Magnetic helicity transport in the advective gauge family*, *Physics of Plasmas* **18** (2011) 012903 [1010.6177].

[32] I. Rogachevskii, O. Ruchayskiy, A. Boyarsky, J. Fröhlich, N. Kleeorin, A. Brandenburg et al., *Laminar and Turbulent Dynamos in Chiral Magnetohydrodynamics. I. Theory*, *Astrophys. J.* **846** (2017) 153 [1705.00378].

[33] J. Schober, A. Brandenburg, I. Rogachevskii and N. Kleeorin, *Energetics of turbulence generated by chiral MHD dynamos*, *Geophysical and Astrophysical Fluid Dynamics* **113** (2019) 107 [1803.06350].

[34] Pencil Code Collaboration, A. Brandenburg, A. Johansen, P. Bourdin, W. Dobler, W. Lyra et al., *The Pencil Code, a modular MPI code for partial differential equations and particles: multipurpose and multiuser-maintained*, *J. Open Source Software* **6** (2021) 2807 [2009.08231].

[35] P. Arnold, G.D. Moore and L.G. Yaffe, *Transport coefficients in high temperature gauge theories (I): leading-log results*, *Journal of High Energy Physics* **2000** (2000) 001 [hep-ph/0010177].